

SYNOSIS: Image synthesis pipeline for machine vision in metal surface inspection

✉ Juraj Fulir*, *Fraunhofer ITWM*, Kaiserslautern, Germany

Natascha Jeziorski, *RPTU Kaiserslautern-Landau*, Kaiserslautern, Germany

✉ Lovro Bosnar, *Fraunhofer ITWM*, Kaiserslautern, Germany

✉ Hans Hagen, *RPTU Kaiserslautern-Landau*, Kaiserslautern, Germany

✉ Claudia Redenbach, *RPTU Kaiserslautern-Landau*, Kaiserslautern, Germany

✉ Petra Gospodnetić, *Fraunhofer ITWM*, Kaiserslautern, Germany

Tobias Herrfurth, *Fraunhofer IOF*, Jena, Germany

Marcus Trost, *Fraunhofer IOF*, Jena, Germany

Thomas Gischkat, *Fraunhofer IOF*, Jena, Germany

Abstract—The use of machine learning (ML) methods for development of robust and flexible visual inspection system has shown promising. However their performance is highly dependent on the amount and diversity of training data. This is often restricted not only due to costs but also due to a wide variety of defects and product surfaces which occur with varying frequency. As such, one can not guarantee that the acquired dataset contains enough defect and product surface occurrences which are needed to develop a robust model. Using parametric synthetic dataset generation, it is possible to avoid these issues. In this work, we introduce a complete pipeline which describes in detail how to approach image synthesis for surface inspection - from first acquisition, to texture and defect modeling, data generation, comparison to real data and finally use of the synthetic data to train a defect segmentation model. The pipeline is in detail evaluated for milled and sandblasted aluminum surfaces. In addition to providing an in-depth view into each step, discussion of chosen methods, and presentation of ML results, we provide a comprehensive dual dataset containing both real and synthetic images.

Index Terms—synthetic data, defect recognition, surface texture, surface inspection, machine vision, domain generalization

I. INTRODUCTION

Machine vision is used to automate repetitive processes which rely on visual information. As such, it has many uses in industrial applications. Processes such as visual quality inspection would otherwise be performed either by humans or might not even be performed at all in cases such as extreme working environments (temperature, noise, chemicals, etc.). Albeit being very flexible in terms of variety of possible applications, every machine vision solution on its own is highly specialized, integrates expert knowledge and cannot be easily adapted if inspection requirements or production environment change.

Automated visual inspection systems (further referred to as inspection systems) are currently developed in a manner which requires the rigidity to ensure reliable performance [1]. This further reduces the flexibility and customization capabilities of production lines, which are ever more required. As a mean to reduce the rigidity, the integrators of inspection

systems are turning towards machine learning (ML) techniques for machine vision. While the ML solutions have showed promising, their reliability and flexibility over longer periods of time is yet to be proven, making the industry skeptic towards their integration into production lines. Additionally, machine learning requires a significant amount of training data, which has shown to be challenging for industrial inspection systems. The inspection tasks are typically very specific and there are little to no publicly available datasets [2]. Therefore, a dataset must be created for each new system. This is not only costly and time consuming, but also poses a significant challenge to generate a well balanced dataset.

The use of synthetic data for ML is rapidly gaining popularity [3]. When it comes to its use in inspection systems, isolated studies have been performed providing evidence of its benefit. However, to date there is a lack of commonly agreed upon best practice or a more comprehensive evaluation of different steps required to generate a photorealistic synthetic dataset for visual inspection. Furthermore, inspection datasets containing both real and synthetic images of the same task are scarce. Such datasets are needed to help establish benchmark performance and support further research and result comparison on the use of synthetic data for visual inspection.

In this work we address the above-mentioned gap by presenting the **SYNOSIS¹ pipeline**. As illustrated in fig. 1, the pipeline includes 1) surface measurement and parameterization, 2) generation of physically correct synthetic images through parameterization of surface, defects and acquisition environment, 3) evaluation of synthetic image quality, and 4) their use for surface inspection ML. For the purpose of this work, the chosen inspection use-case focused on milled and sandblasted metal surfaces without coating. However, the pipeline is developed to be applicable for a wide variety of materials and defects, and, for the first time, introduces **decomposition of different geometry scales** in inspection context. Finally, we **publish a dual dataset²** for defect recognition containing real and synthetic image pairs acquired

¹Synthetic, optically realistic images for ML-based inspection systems

²Dataset is publicly available at: <http://dx.doi.org/10.24406/fordatis/370>

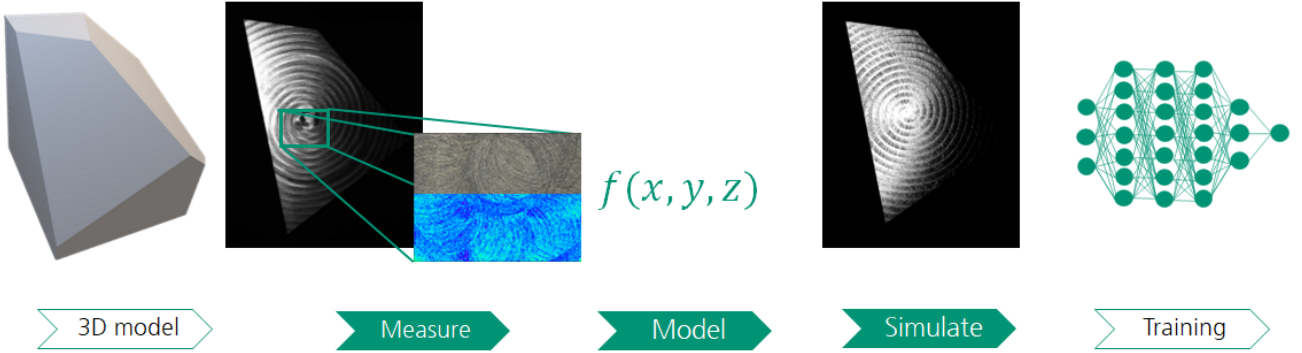


Fig. 1: SYNOSIS synthesis pipeline. Based on a **3D model** of an object, spatial properties of the surface texture are **measured**. Surface topography and manufacturing parameters are used to develop a **mathematical model** capable of reproducing the texture as a normal map. Multiple realizations of the texture are generated by varying the parameters and are applied onto the 3D model of the object which has been altered to include surface defects of varying types and sizes. During the **simulation** step, the final image is computed based on the interaction between the acquisition environment (light, camera), object geometry and texture normal map. This process is repeated an arbitrary amount of times. Parameters defining texture and surface defects are varied to generate a **training dataset** which is sufficient in terms of both image quantity and content variance.

and simulated for corresponding parameters.

A. Paper Structure

The content is grouped into 8 sections and contains bolded keywords to make the reading easier. The generation process needed to obtain synthetic images for surface inspection is covered in section II. There we provide an overview of the related work, introduce inspection relevant decomposition of scales, and discuss the most important elements of the generation process and their relation to different scales. Sections III and IV introduce methods chosen to produce test object surfaces in a controlled manner and measure surface topography. Sections V and VI focus on texture and defect modeling as the most relevant aspects which need to be controlled when creating synthetic data for surface inspection. Section V discusses different approaches which can be taken to represent surface texture and their benefits or shortcomings. Further, the section introduces stochastic geometry modeling approaches used to the specific surfaces found in our specific use-case. Section VI discusses different approaches to defect generation in the related work, and provides an overview of the defect modeling workflow used for our specific use-case. Section VII introduces how was both real and synthetic data obtained. For synthetic data it explains how was the synthetic image generation process (introduced in section II) used and with which parameters to create the synthetic dataset. Finally, section VIII provides a discussion of different means which can be used to evaluate the quality of the created synthetic dataset and their results when applied to our use-case.

II. SYNTHETIC DATASET GENERATION

A. Related work

The goal of **synthetic image data generation** is to generate image datasets where image characteristics are ideally the same as those of images acquired in reality. The characteristics

include both appearance and content distribution. When there is a discrepancy between the synthetic and real images in terms of their characteristics, it is referred to as *domain gap*.

Early, straightforward, approach to extending training datasets was to add defect textures to images of defect-free surfaces [4]. The defects are 2D image patches which cannot correctly represent light interaction and have inconsistent appearance with respect to the rest of the surface. Due to the nature of the approach it is very difficult to enhance it in a way which would minimize the resulting domain gap. Therefore, further synthetic data efforts were aimed at **generative** methods, based on predominantly deep learning, and **rule-based** approaches, using computer graphics simulation based on a well-defined set of rules which describe the imaging context [5].

The high degree of complexity when generating photorealistic surface features caused many of the authors to adopt the **generative approach**, focusing on defect generation. Jain et al. [6] compare the performance of three different GAN architectures for generating defects in hot-rolled steel strips. Defect-GAN [7] was introduced for automated surface defect synthesis by mimicking the defacement and restoration process and capturing stochastic variation of defects. Defect-Transfer GAN [8] is trained over multiple products with similar defects in order to enable introduction of semantically new information and make up for the limited availability of all possible object attributes in the real dataset. Wei et al. [9] generate defect patches and blend them into a clean image, thus being able to obtain approximate segmentation masks. These approaches are more suitable for generating large defects which visibly differ from the surrounding surface and do not suffer if image is resized to lower resolution for inference performance reasons. As such they can be expected to struggle when confronted with surface containing texture pattern whose appearance has prominent local variation, as is the case for milled surfaces. Schmedemann [10] explored a hybrid approach by applying



Fig. 2: Examples of the three textures considered in this paper: surface finishing by sandblasting, parallel milling, and spiral milling.

style-transfer on images generated by a rule-based approach to obtain more control and reduce the *domain gap*. It has shown that this approach can lead to a loss of features making it not reliable without a human operator review of the generated images.

Generative deep learning approaches may result in images which look realistic but also incorporate errors on a level which is beyond our comprehension, further causing misalignment when that data is used for training. Also, the generative methods do not know anything about the context or what has caused an image to appear in a particular manner. Hence, it is difficult to control the dataset content and the distribution of features within. That said, they cannot introduce edge-case scenarios or guarantee correct data generation. This problem can be partially circumvented only by retraining on new data containing the desired features.

Rule-based image synthesis relies on computer graphics for modeling and rendering **virtual environments** which have recently gained popularity beyond the entertainment industry (e.g., movies or gaming). It represents a controllable, versatile and reliable approach for generating arbitrary amounts of data with customized features and variations. As such, it has proven useful across various machine vision tasks as discussed by Dahmen et al. [11]. Synthetic data are currently predominantly used in the human-oriented domains, autonomous driving and robotics, see [12].

Human-oriented synthetic data is used in tasks which include body tracking and pose estimation [13]–[15] or face recognition [16]. Synthetic data for autonomous driving relies on virtual environments of large-scale urban and traffic scenes [17] for recognition tasks [18] and object detection [19]. The robotics domain requires virtual environments [20], [21] for recognition tasks such as semantic segmentation [22] and object detection [23]. In all three domains, the focus is on large scale geometric features while simulation of small scale details and textures is not necessary.

Surface inspection belongs to industry automation, which is closely linked to robotics, but includes tasks beyond those needed for movement, localization and mapping. In particular, building virtual environments for inspection planning and the

development of defect recognition algorithms require a high level of realism and small-scale surface details. This makes this domain highly different from the domains discussed above.

A general-purpose dataset generator is introduced by Greff et al. [24]. It promises realism (using physically-based ray tracing), scalability and reproducibility which are also covered by our pipeline. However, being a general framework, it requires a user to define a 3D scene for the particular task using scripting. Assets for the 3D scene must be either created by the user or imported from general-purpose asset libraries. As such, data generation for specialized problems, such as quality assurance, is challenging due to unavailable assets, assets with unsatisfactory features or limited modeling capabilities of a user.

Moonen et al. [25] presented a toolkit for synthetic image data generation in manufacturing. Synthesizing datasets for industrial inspection using a rule-based approach was further discussed in [26]–[30]. Synthetic data was further used for various quality assurance tasks such as inspection of industrial components [31], metal surface inspection [32], industrial visual inspection [33], scaffolding quality inspection [34] or viewpoint estimation [35]. Raymond et al. [36] introduced models of scratched metal surface where they stacked layers containing different scratch distributions. However, their model does not represent curving scratches nor dents or scratches with varying geometrical depth. None of the mentioned works provide the level of control introduced by Bosnar et al. [37] with parameters designed to separately control image acquisition context, texture appearance and defect characteristics.

The work presented in this paper builds on the virtual inspection planning research done by Gospodnetić [38] and Bosnar et al. [37], [39], [40]. Bosnar et al. [37] identified core computer graphics components needed to perform image synthesis for surface inspection and stressed the importance of texture and defect parameterization to minimize the need for artistic approach. However it focused mainly on the concepts and not challenges which arise when applying it to a realistic scenario. We extend the aforementioned pipeline and apply it to a realistic scenario. Procedural textures and defects

for generating synthetic data for defect recognition in visual surface inspection were introduced in [39], [40]. Their defect modeling approach was also adopted by Schmedemann et al. [41] for the rule based generated images before application of style transfer. Fulir et al. [42] also built on top of [37], [39], [40] to produce a synthetic dataset for defect segmentation on metal surfaces but discussed mainly ML results.

B. Decomposition of Scales

A 3D scene contains **3D objects** which are traditionally decoupled into geometry and material. The geometry specifies the size, position and shape of an object (high-level appearance), while the material influences how the light interacts with its surface (detailed appearance). Alternatively, a 3D object can be considered at three different scales: macro, meso and micro scale. The **macro scale** refers to object geometry (e.g., represented by a mesh) and large geometrical features such as defects. **Meso scale** refers to the surface structure on a much smaller scale than the shape of the object, but larger than the wavelength of light (i.e., surface texture), as discussed by Dorsey et al. [43, ch. 2]. **Micro scale** refers to the surface structure and properties which are not separately distinguishable by the imaging sensor, but are contributing to light reflection.

It is difficult to make a strict distinction between the scales using units, because the scales are relative to the imaging sensor resolution and viewing distance. Therefore, we propose the following guidelines. The macro scale should be attributed to geometrical shapes which take larger portions of the image. The micro scale can be determined using the Nyquist-Shannon sampling theorem [44] stating that *the sampling rate must be at least twice the bandwidth of the signal*. In other words, every feature which cannot be sampled by more than one pixel falls under the micro scale class. Finally, the meso scale constitutes features which occupy a smaller but visible portion of the image, measured in a handful of pixels.

To give some examples, assume we were to observe an outdoor scene of a park containing people and trees. Then the shapes of people and trees would make the macro scale, whereas the eyes or leaves would already fall under the meso scale, and the skin or the leaf veins would be considered micro scale. In the case of visual surface inspection, we are looking at specific parts of an object with high resolution. Therefore, the inspected object is in the macro scale, its defects and surface texture caused by the manufacturing process are in the meso scale, while roughness and smallest surface features are part of the micro scale.

C. Rule based image synthesis

Rule based image synthesis (fig. 3) can be divided into two main steps: 3D scene modeling (i.e., modeling of the virtual environment) and rendering procedures as discussed by Greenberg et al. [45] and Tsirikoglou [12]. During rendering, the 3D scene is used to generate 2D images. The crucial element for achieving realism of those images is physically-based light transport, using path-tracing (Kajiya [46], Pharr et al. [47]). In this work, we use appleseed [48] rendering engine which implements these principles.

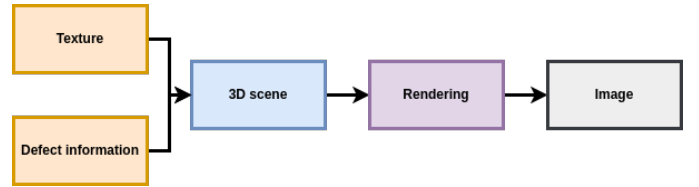


Fig. 3: Image synthesis overview. Texture and defect information is joined with the 3D scene to perform rendering and generate an image. The defect information is varied to perform photo-realistic image synthesis of both defected and defect-free object instances. In case of defected instances, pixel-precise defect annotations are automatically created.

D. 3D scene modeling

The **3D scene** represents the real world context within which the images are acquired. As such, the scene to be simulated must faithfully represent the environment. For surface inspection this includes 3D objects, lights and cameras. Note that we do not necessary include environment illumination, since inspection systems often have a strictly controlled acquisition environment and no uncontrolled illumination. While all the components contribute to the image realism, in this work we focus on the realism of the 3d object, influenced by the geometry, material and surface topography (i.e. texture).

The **geometry** of the 3D models representing the inspected object (macro scale) must correspond to the geometry of the real inspected product. In this work we use the 3D model of *test bodies* (section III) and create defected product instances by augmenting defects (meso scale) directly into the product geometry [40]. This is done because the defects are larger than the surface texture, and their complex shape causes intricate light scattering that can not be captured by normal maps alone, as described in section VI.

Material properties describe the light-surface interaction and are modeled the bidirectional reflectance distribution function (BRDF) as discussed by Dorsey et al. [43]. For this work, rough metal surface BRDF is used (Walter et al. [49], Kulla et al. [50] and Turquin et al. [51]). The BRDF is evaluated in every surface point based on the local surface normal. Unrealistically smooth surface is avoided through variation of BRDF parameters and normals using texture.

Texture is a term for which the exact definition differs across domains. Here we refer to the computer graphics concept which defines it as a procedure to introduce the surface topography by influencing (perturbing) the surface normal and BRDF parameters for every surface point at rendering time (Mikkelsen et al. [52]). As such, the texture describes the meso scale surface patterns, which would otherwise be very inefficient to be represented by the geometry. The section V offers a more complete overview of the texture modeling approaches. Traditionally, texture modeling is aimed to be used by artists to approximately recreate photorealistic visual appearance and enable their creative expression (Guerrero et al. [53], Adobe Substance [54], Ebert et al. [55]). Therefore, the surface models are based more on artist oriented parameters, rather than the real-world parameters, making

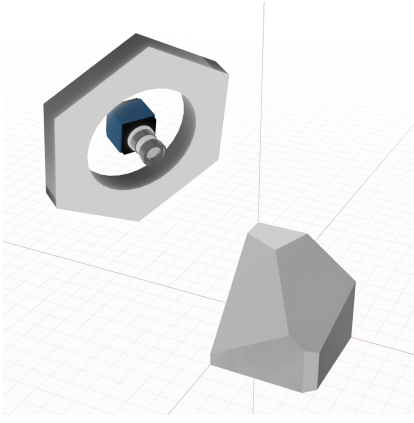


Fig. 4: Simulated 3D scene representing the real inspection environment.

them visually appealing but not necessarily correct. Dong et al. [56] approached realism by fitting a gaussian random field to surface measurements and using it as texture. It gave impressive results for a single instance of measurements, but offered no further control over the pattern properties.

In contrast to [56], we recreate the surface measurements using mathematical models which can be controlled based on real-world parameters (see section V). The textures are generated as 2D images encoding the normal variation, which are then mapped onto the surface of the object as explained in section II-E. Given the high level of details produced by the models, we keep the BRDF roughness parameter fixed to a constant small values (e.g., within a range (0.0-0.1)).

Light in the 3D scene represents the illumination devices used in the surface inspection environment. We use a model of the ring light geometry used in the real inspection system which has a torus-like shape (fig. 4) with diffuse emission distribution describing the light emission in each point of the shape. As in the real setup, the camera is placed in the center of the ring with both objects having the same orientation.

The **camera** is using a pinhole camera model defined by its resolution, pixel size, focal length, position and orientation parameters. Simulated camera parameters are set to resemble the real camera parameters used in the surface inspection environment. The pinhole model does not account for the depth of field or optical aberrations such as distortions. For the purpose of this work, this is sufficient since the inspected surface is expected to be in focus and effects such as image distortion or global blurring can be introduced in post processing or during training in form of image augmentations.

E. Texture mapping

The textures used in this work are represented as normal map images where each pixel encodes a normal vector. While [57] suggests that the implicit procedural generation is ideal, it requires an additional level of restrictions and complexity when developing the new models. In particular, it is the limited spatial information which makes describing spatially-varying patterns with regular global structures such as the milling patterns in the physical test bodies (fig. 2) challenging. While

the implicit implementation is possible, it is outside the scope of this work in order to allow focusing on physically realistic texture modeling.

In order to use the texture images together with BRDF evaluation during rendering, it is required to map them onto the 3D object. Typically either it is done by using projection directly [47] (e.g., planar, cube, spherical) or by unwrapping the object [58] (i.e., mapping the object faces to a plane). Applying the texture projection directly onto the whole object will cause artifacts such as texture stretching for complex geometries. This is not acceptable for generating synthetic training data. Therefore, in this work we first separate the geometry into main planar surfaces and then use planar projection separately per surface. To avoid the occurrence of texture tiling (visible repetition in pattern), the texture images are generate large enough to cover the entire target surface.

F. Rendering

The 3D scene description is used to render the synthetic images from all given camera positions. The main rendering parameters influencing the quality of synthesized images are the number of samples per pixel (SPP) and the number of light ray bounces.

In surface inspection each pixel covers rich and complex surface structure. Higher SPP ensures that the computed pixel color is a good approximation of the mean light response value of the covered area. As such, increasing the number of SPPs will reduce noise and aliasing in the rendered image.

In addition to texture, our 3D objects contain defects in form of small, complex, geometrical features. Increasing the number of light bounces (i.e., times the ray is allowed to bounce off the intersection point) enables to represent the complex light phenomena such as shadowing, masking or interreflections. This phenomena can not be correctly represented using normal maps alone.

G. Defect annotations generation

The object geometry used in the 3D scene is defected using methods based on work by Bosnar et al. [40]. Each imprinted defect geometry has the corresponding geometrical defect mask section VI. Black (non-emissive) material is applied on the 3D object, emissive material is set to the geometrical masks and all light sources are disabled. Finally, the annotations are generated using the same camera parameters as for the corresponding photorealistic image, which ensures pixel-precise labels of the defect areas visible from the camera position and not occluded by the 3D object. This approach is introduced by Bosnar et al. [40] and will always generate defect annotations regardless of their light response, as can be seen in fig. 6.

III. TEST BODY DESIGN

Injection of the domain knowledge is crucial for developing photorealistic models. Therefore, we use custom designed and manufactured test objects, giving us complete insight into and control over the processing chain. This allows us to focus on the image synthesis, surface modeling, dataset generation and training challenges.

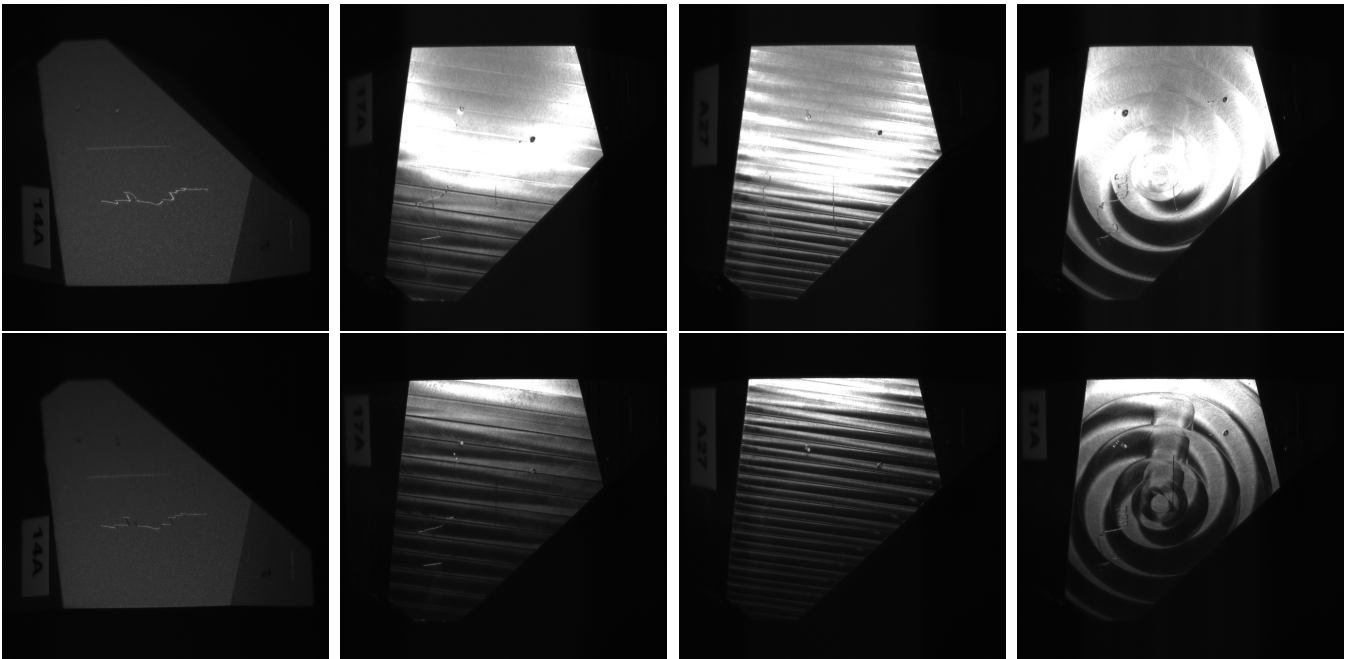


Fig. 5: Real images of object surface with defects. Top row: 20 degrees angle from perpendicular view. Bottom row: 40 degrees angle from perpendicular view.

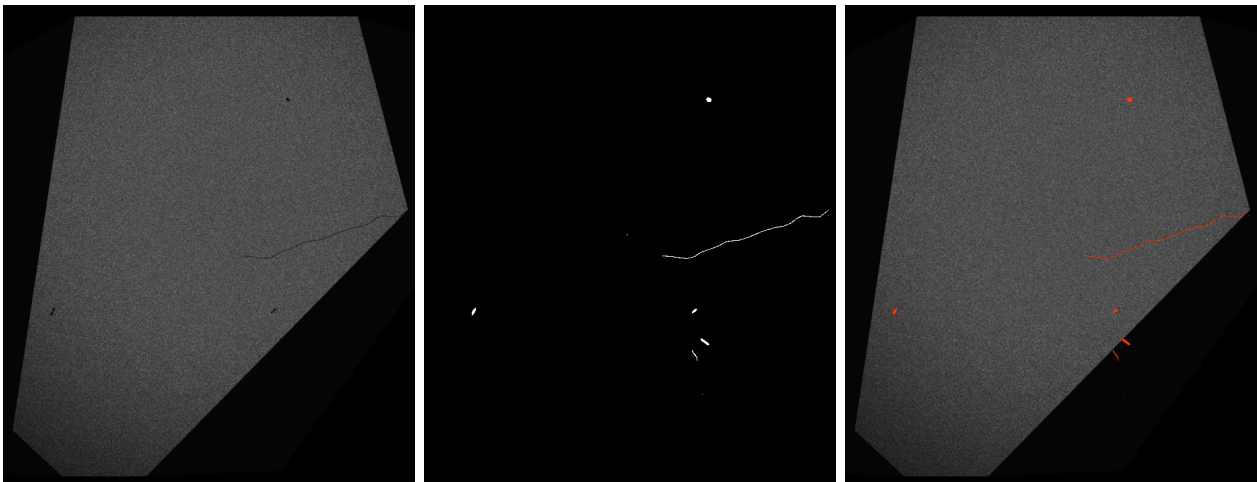


Fig. 6: Left: defected synthetic image. Middle: defect annotations. Right: defected synthetic image with annotations overlay.

In total, three identical sets of test objects were fabricated, each containing 10 polyhedral test bodies. When designing the test bodies, the aim was to generate bodies with multiple faces showing different realistic surface texture patterns.

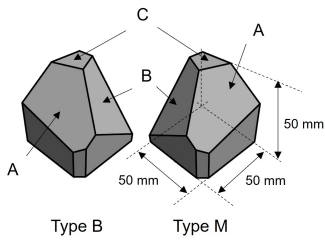
The base bodies (type B and type M) are polyhedrons made from aluminum, see fig. 7a. Each polyhedron has size $5\text{ cm} \times 5\text{ cm} \times 5\text{ cm}$ with planar faces A, B and C of approximately size $2\text{ cm} \times 2\text{ cm}$ which are measured and modeled subsequently. The remaining faces are left “unfinished” (rough milling) and are not further considered. The difference between type B and type M is the mirrored arrangement of the faces of the base body.

First, the surfaces are milled using different processing parameters (fig. 7b). A rotating cutter with a specific head diameter is used to remove material from the surfaces by

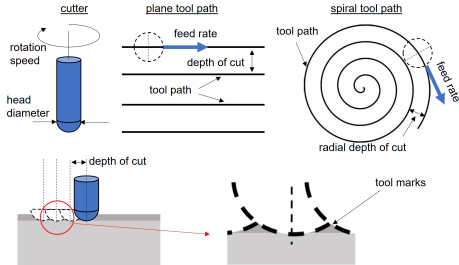
performing many separate, small cuts along the tool path with a defined feed rate. We consider face-milling, which means that the tool moves perpendicularly to the object surface. The distance between the neighboring tool paths depends on the radial depth of the cut and influences the resulting tool marks, see fig. 7c. Parallel linear and spiral tool paths are used. Artifacts in form of exit lines can occur for spiral milling.

After milling, some of the faces were sandblasted, a process in which a hand-held nozzle of a sandblasting tool blasts the surface with a mixture of sand and air at high pressure. This abrasive method can smoothen or roughen the surface. The resulting surface topography depends thus on the pressure of the air jet, the grain size distribution, shape and material of the sand.

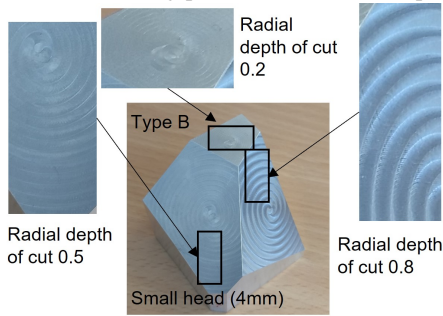
The parameter values of both processing techniques (see



(a) Drawing of the base test bodies.



(b) Sketch of the milling processes and its main parameters.



(c) Picture of the manufactured surfaces of type B spiral milled with a small head (4 mm) and various radial cutting depths.

Fig. 7: Illustration of the test object used in the project, the milling processes and a test object with milled surfaces.

Technique	Parameter	Values
milling	milling head diameter	4 mm, 8 mm
	radial depth of cut	0.2, 0.5, 0.8
	path	parallel, spiral
sandblasting	pressure	2.5 bar, 6 bar

TABLE I: Used parameter settings for processing.

table I) were chosen to result in realistic patterns expected to emerge from industrial processing.

Objects in set 1 contain no surface defects, while sets 2 and 3 contain more than 200 scratches and localized point defects, created precisely on the faces. For this purpose, a custom “indenter” and a scratch test tool were used where the tips can be loaded with different masses. As tips we used a diamond tip, a steel needle and a screw. The load of the tips were 500 g, 1000 g and 1500 g. Using the tools, the scratches (straight and free-form lines) and digs (dents) are realized on the surfaces as typical surface defects in accordance to ISO8785. The generated defect sizes were in the range of sub-millimeter to millimeter. See fig. 8 for an example of defect specification.

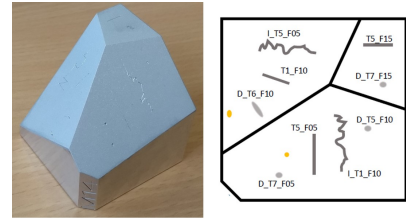


Fig. 8: Test object type M after sandblasting and subsequently introduced defects with different types and sizes.

IV. MATERIAL MEASUREMENTS

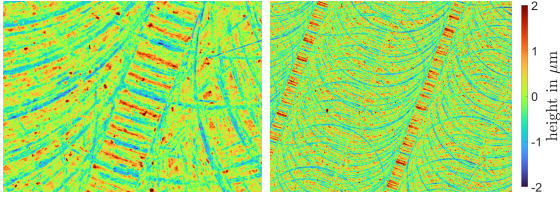
In order to characterize the machined surfaces, optical 3d and topography measurements are performed by means of focus-variation microscopy (Bruker alicon a InfiniteFocus G4). In the high precision machining industry measurement systems based on the focus-variation technique are standard inspection tools to characterize 3D mechanical parts. The advantage is the high precision and contact-free measurement of roughness, surface structure, micro-geometry and form using one optical sensor. The measurement system is based on a precise optical lens system with shallow depth sharpness. By changing the working distance between the measured surface and the microscope lens, different depths of the surface come into focus and are projected sharply onto the sensor. The proprietary software analyzes the distance for each point and measures the sharpness, which is used for the calculation of the surface depth profile (topography).

Depending on the magnification of the optical lens system, this process allows a vertical resolution down to 10 nm (magnification equivalent of 100x, which is a physical magnification limit). For the purpose of this work, an optical lens system with a magnification of 5x and a nominal vertical resolution of 410 nm is used. The vertical resolution was limited during data acquisition by the measurement software. The defect free samples of objects in test set 1 are measured with different lateral resolutions, depending on the size of the scanned surface area, as it is shown in fig. 9. The topography measurements are converted into ASCII xyz-files in order to create readable files used for surface modeling. This results in height images, where each pixel is assigned a height value.

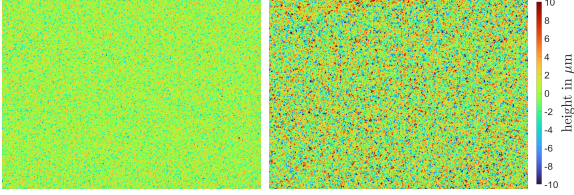
Depending on the process parameters, the tool marks created by the milling process form a unique pattern which can be observed by the naked eye (fig. 7c) and influences the subsequent surface light response, playing the key role in surface inspection. Measurements of surfaces processed using different parameter settings are given in fig. 10.

When sandblasting, the previous milling does not affect the final surface pattern, see fig. 9b. The process results in a homogeneous surface texture without long scale spatial relations.

In order to characterize the generated defects we used an optical lens system with a magnification of 20x and manually adjusted the vertical resolution during data acquisition through the software. Depth quality filter value was set between 2×10^{-6} and 8×10^{-6} , depending on the defect type and size (e.g., fig. 11). The shape of the dent resembles a dig with a

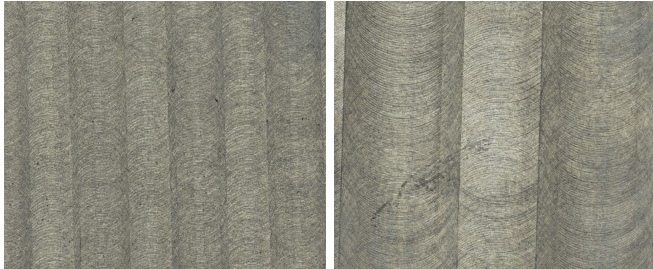


(a) Parallel milled surface using milling head diameter 4 mm and radial depth of cut 0.5. Small imaged region (left) is $2 \text{ mm} \times 1.4 \text{ mm}$ with pixel size $0.44 \mu\text{m}$ and large imaged region (right) is $7.5 \text{ mm} \times 5.9 \text{ mm}$ with pixel size $1.75 \mu\text{m}$.

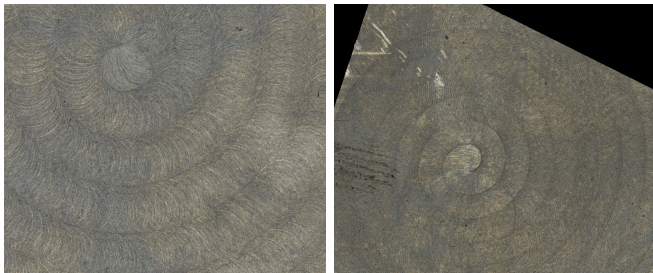


(b) Sandblasted surface using pressure 2.5 bar (left) and 6 bar (right). Imaged region is $7.7 \text{ mm} \times 5.7 \text{ mm}$ with pixel size $1.75 \mu\text{m}$.

Fig. 9: Topography measurements of sandblasted and milled surfaces.



Parallel milling, head diameter 4 mm, radial depth of cut 0.8. Parallel milling, head diameter 8 mm, radial depth of cut 0.8.



Spiral milling, head diameter 4 mm, radial depth of cut 0.5. Spiral milling, head diameter 8 mm, radial depth of cut 0.2.

Fig. 10: Optical 3d measurements of milled surfaces using different parameter settings. Imaged region is $21 \text{ mm} \times 17.5 \text{ mm}$ with pixel size $7 \mu\text{m}$.

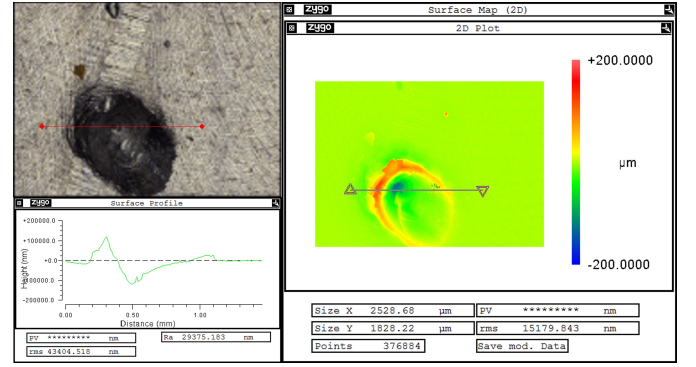


Fig. 11: Optical 3d (top left) and topography (right) measurement with 2d intersection of the height profile (bottom left) marked in the topography measurement of a defect created using the indenter with load of 500g.

peak and a valley of about $150 \mu\text{m}$ in height and depth with respect to the undamaged surface level.

V. TEXTURE MODELING

Due to the very different surface topographies (fig. 9), separate models are required for sandblasted and milled surfaces. Models are selected based on the corresponding topography measurements \mathcal{M} , and used to simulate the meso scale of the object (texture).

Measurements of the test body surfaces are provided as 2D height images $\mathcal{M} : \{1, \dots, M_{\mathcal{M}}\} \times \{1, \dots, N_{\mathcal{M}}\} \rightarrow \mathbb{R}$ of size $M_{\mathcal{M}} \times N_{\mathcal{M}}$ for $M_{\mathcal{M}}, N_{\mathcal{M}} \in \mathbb{N}$ and pixel spacing $\nu_{\mathcal{M}} \in \mathbb{R}_{>0}$. The output of the models is a texture image \mathcal{T} of arbitrary size $M_{\mathcal{T}} \times N_{\mathcal{T}}$ and pixel spacing $\nu_{\mathcal{T}} \geq \nu_{\mathcal{M}}$ coarser or equal to the input's pixel spacing. For the purpose of this work, we use $\nu_{\mathcal{T}} \approx 6.1 \mu\text{m}$ and $M_{\mathcal{T}} = N_{\mathcal{T}} = 13107$ so that a squared imaged region with edge length 80mm is provided. The chosen pixel spacing is large enough to generate images of appropriate size for which the rendering process can still be done in acceptable time. On the other hand, pixel spacing is chosen small enough so that no visible discretization artifacts occur. The resulting texture image can completely cover test body surfaces during the rendering process, even when the texture image is rotated. This way, image tiling is avoided as it may produce visible edges between the tiles.

A. Related work

In computer graphics, the textures representing surface topographies can be roughly separated into procedural and data-based, see fig. 12. In this work we used explicit procedural for the milling texture and exemplar-based approach for the sandblasted texture.

Procedural texture modeling is based on algorithms which completely describe the surface patterns without the need for additional data (e.g., image data). The main concept is to combine regular patterns (e.g. sine functions, simple shapes such as lines and circles as well as other mathematical functions) discussed by Vivo et al. [59] with irregular patterns (e.g. noise functions) discussed by Dong et al. [60]. Since procedural

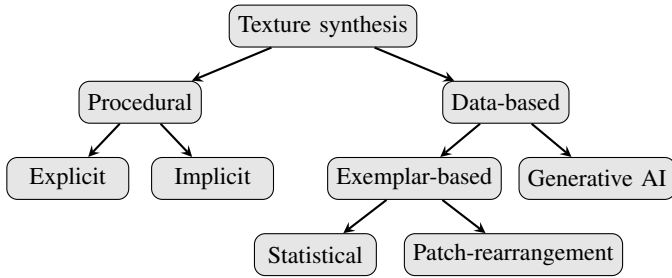


Fig. 12: Classification of computer graphics methods for texture synthesis.

texture models are algorithmic descriptions of a texture, they offer parameterization and thus immense controllability which is recognized by the computer graphics community for content creation [61]. However, developing procedural textures is often done by artists who base their work on experience and expression rather than encoding physically correct parameters.

Deguy [61] separates procedural models into implicit and explicit. An **explicit** procedural texture model generates a texture image which is first mapped onto the object surface and then used during rendering. Contrary, an **implicit** procedural texture model is directly evaluated during the rendering procedure, thus generating texture in render-time and allowing render-time re-parametrization. While explicit procedural models are easier to develop for complex texture patterns, implicit procedural texture models can cover arbitrarily large surfaces without repetitions or seams and are not restricted by the resolution. Bosnar et al. [39] developed implicit procedural texture models for circular, parallel and radial textures. Those patterns resemble processed surfaces but without taking an explicit machining method into account or basing them on real surface topography.

Data-based texture modeling relies on sensor data and measurements as input, as discussed by Tsirikoglou et al. [12]. For example, the input texture image may be obtained using photogrammetry [62] or other scanning techniques [63].

The advantage of data-driven texture modeling is that it can synthesize approximations of real-world surfaces for which there are no well-defined mathematical descriptions. However, those methods offer little control over the generated content since they depend entirely on the input data. Data-based texture modeling can be roughly separated into generative AI and exemplar-based approaches. **Generative AI texture synthesis** is often based on GANs as discussed by Jetchev et al. [64], Bergmann et al. [65] and Zeltner et al. [66]. While the results of these models often have remarkable appearance to a person, it is not possible to ensure that the results are physically correct and is very difficult to introduce controllable parameters for different kinds of textures. **Exemplar-based texture synthesis** uses algorithms to generate new texture images similar to a given input image. While stationary textures can be well reproduced, problems occur for textures with complex, large structures, e.g. milling rings.

Furthermore, since the output image relies entirely on the input image, it leaves no possibility of influencing the pattern itself. Raad et al. [67] give an overview of common exemplar-

based texture synthesis methods. They distinguish between statistical and patch-rearrangement methods.

Statistical exemplar-based methods perform two steps. First, model-dependent statistics of the input image are computed. Second, a randomly initialized image is adjusted such that it fits the observed statistics. The asymptotic discrete spot noise (ADSN) and the random phase noise (RPN) are both parameter-free and non-iterative statistical methods [68]. A texture image simulated by the ADSN maintains the mean of the input image but has minor differences when comparing the sample auto-correlation since its Fourier modulus is the Fourier modulus of the input image multiplied by Rayleigh noise. The RPN creates texture images that have the same Fourier modulus as the input image and thus the same auto-correlation but a random Fourier phase. Heeger and Bergen [69], [70] introduced a procedure for texture modeling that uses image pyramids. A random image is adjusted iteratively by matching histograms of all images in its image pyramid to the corresponding images in the image pyramid of the reference image. Portilla and Simoncelli [71], [72] improved this method by using statistics such as cross-correlations between pyramid levels, instead of histogram matching. In contrast to the exemplar-based methods that generate completely new texture images, the **patch-rearrangement methods** quilt patches taken from the input image. With the method of Efros and Freeman [73], [74], the output image grows successively by adding certain patches one after the other in a raster-scan order. It is an extension of the method of Efros and Leung [75] that generates a new texture image pixel by pixel.

Guehl et al. [76] introduce a hybrid approach combining procedural and data-based texture synthesis. The visual structure of the generated image texture is based on a procedural parametric model, while texture details are synthesized using a data-driven approach. Another hybrid approach is presented by Hu et al. [77], in which the texture of the input image, which contains the BRDF parameters, is decomposed and proceduralized.

Modelling of metallic surfaces in computer graphics has received a lot of attention. Particularly interesting methods are the ones describing highly specular surfaces with high-frequency details (glints) discussed by Zhu et al. [78] and Chermain [79]. Glint effects appear due to complex and unstructured small-scale, high-frequency geometries such as tiny bumps, dents and scratches. The problem with these approaches is that they do not model the actual properties of surfaces to resemble any particular and standardized surface. Rather, they are modeled to resemble the surface finishing appearance in an artistic way which is difficult to compare to any particular real-world counterpart.

Milling belongs to the machining processes resulting in deterministic and describable surface patterns [80], [81]. Therefore it is extremely useful to incorporate existing domain knowledge into texture models for milled surfaces. To estimate the surface quality of milled surfaces and thus determine the required quality, Felho et al. [82], [83] and Kundrak et al. [84] developed models for parallel face-milled surfaces. Hadad et al. [85] developed a more detailed model that takes other typical milling parameters into account, e.g. tilting of

the tool to avoid re-cutting. All models create milled surfaces using CAD software and the patterns are thus geometrically imprinted into the surface. Oranli et al. [86] provide a similar approach to simulate the physical process of sandblasting and the resulting surface deformation in high precision using the Abaqus software. Using such approach in for data synthesis would result in unfeasibly long computation times. Furthermore, the surfaces generated in this way look too perfect, as possible irregularities, e.g. slight deviations in the cutting geometry due to irregular material and machine behavior, are not included in the models.

B. Sandblasted surface

The surface topography shows a different range of height values and degree of roughness depending on the pressure of the air-jet (fig. 9b). The resulting surface topography is homogeneous, resembling a stationary Gaussian random field. However, fitting parametric Gaussian random fields did not provide satisfactory texture images since the structure sizes were not reproduced correctly. In addition, due to the small number of process parameters, it is difficult to develop a model that depends exclusively on them. Therefore, we used a combination of exemplar-based texture synthesis methods that only receive the measurement as input. We select measurements with a size between 4430×3248 and 4440×3288 and pixel spacing $\nu_{\mathcal{M}} \approx 1.75 \mu\text{m}$ that correspond to an area of about $7.8 \text{ mm} \times 5.8 \text{ mm}$.

To generate texture images for sandblasted surfaces, the asymptotic discrete spot noise (ADSN) introduced by Galerne et al. [68] is used. The size and pixel spacing of the input image are maintained. To obtain a new texture image by simulating the ADSN, sample from the multivariate normal distribution $\mathcal{N}(\hat{\mu}_{\mathcal{M}}, \hat{C}_{\mathcal{M}})$ with $\hat{\mu}_{\mathcal{M}}$ the sample mean and $\hat{C}_{\mathcal{M}}$ the sample covariance matrix of the input image.

Next, the desired size $M_{\mathcal{T}} \times N_{\mathcal{T}}$ and pixel spacing $\nu_{\mathcal{T}}$ of the texture image have to be met. The pixel spacing can be adjusted by downsampling the input image using nearest neighbor interpolation. ADSN can generate texture images larger than the input image, while maintaining the same pixel spacing [68]. Therefore, the normalized input image $\sqrt{M_{\mathcal{T}}N_{\mathcal{T}}/M_{\mathcal{M}}N_{\mathcal{M}}}(\mathcal{M} - \hat{\mu}_{\mathcal{M}}) + \hat{\mu}_{\mathcal{M}}$ is enlarged using padding with mean value $\hat{\mu}_{\mathcal{M}}$ before applying the ADSN. However, periodical repetitions are visible in the resulting texture. To avoid this, multiple texture image patches are generated and stitched using EF-stitching [73], [74]. To stitch two neighboring patches within an overlap region, both are cut apart along an intersection edge first and put together afterwards. The intersection edge is determined by finding the path within the overlap region where both images are most similar. Depending on the alignment of two neighboring patches we distinguish between vertical, horizontal and L-shaped stitching (fig. 13), see [87] for details.

C. Milled surface

The model generating textures of milled surfaces is given as a function in a continuous domain \mathbb{R}^2 . Thus, it is procedural but implemented explicitly for the sake of simplicity. The

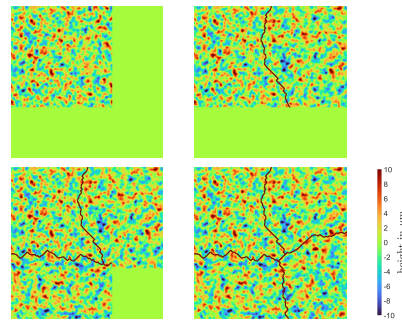
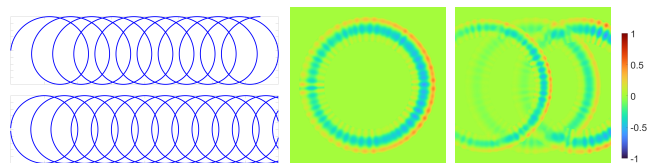


Fig. 13: Illustration of EF-stitching marking the minimal path in each step. Patches have the size of 512×512 and the overlap region width is 256 pixels. The imaged region is approximately $1.34 \text{ mm} \times 1.34 \text{ mm}$.



(a) Edge path (top) and its approximation (bottom). (b) Sub-models for one ring (left) and interaction of multiple rings (right).

Fig. 14: Overview of model generating milled surfaces.

discrete texture image is obtained by evaluating the function at the image grid-points $(\nu_{\mathcal{T}}x, \nu_{\mathcal{T}}y)$ for $x = 1, \dots, M_{\mathcal{T}}$ and $y = 1, \dots, N_{\mathcal{T}}$. The milling pattern appearance depends on a number of parameters associated with production parameters. The most prominent structures are cycloidal edge paths caused by the rotation of the milling head. They are approximated by $n \in \mathbb{N}$ rings R_1, \dots, R_n (fig. 14a). The model is further divided into the following sub-models for the

- 1) tool path providing the arrangement and order of the rings by defining their center points c_k
- 2) appearance of an individual ring R_k (fig. 14b)
- 3) interaction between neighboring rings (fig. 14b)

for $k = 1, \dots, n$.

The first sub-model generates the ring center points $c_k \in \mathbb{R}^2$ along the tool path. Within this study, either parallel or spiral milling (fig. 15) is considered. First, the respective tool path has to be modeled, together with the distance $\rho \in (0, d)$ between two neighboring sub-paths. The distance is controlled by the amount of ring overlap $\alpha \in (0, 1)$ and the diameter $d \in \mathbb{R}_{>0}$ of the rings, as $\rho = (1 - \alpha) \cdot d$. The diameter of the milling head is crucial for defining the ring diameter and the ring overlap depends on the radial cutting depth a_e by $\alpha = 1 - a_e$. The radial cutting depth defines the distance the tool steps over in relation to the ring diameter. As the blades do not reach the edge of the tool, α is reduced here by taking $\alpha - \gamma$ with $\gamma \in [0, \alpha)$. The ring center points c_k are then modeled by random displacements of points \tilde{c}_k which are computed along the tool path. That is, we sample from a two-dimensional normal distribution $c_k \sim \mathcal{N}(\tilde{c}_k, \Sigma_c)$. The location of \tilde{c}_k is specified by the distance $\delta \in \mathbb{R}_{>0}$ between two center points along the tool path. The distance δ depends

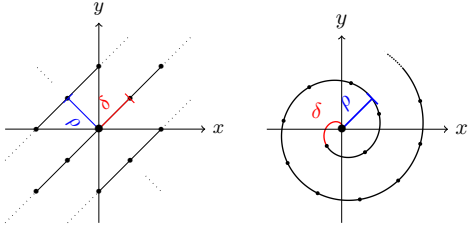


Fig. 15: Tool paths of parallel (left) and spiral milling (right) with center points.

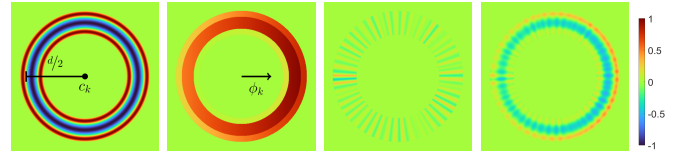
on the tool's feed rate and rotational speed. It is important to keep the chronological order of the rings in order to keep the tool path visible. Finally, while being very precise, the milling process is not perfect and every once in a while there is an occurrence of a ring which is more visible than the others. To introduce such irregularities in visibility of rings, the order of a certain amount $\epsilon \in [0, 1]$ of rings is changed.

The second sub-model controls the appearance of an individual ring R_k , produced by a single rotation of the milling head cutting edge. Therefore, the width of the cutting edge is crucial for the indentation width $w_k^- \sim \mathcal{N}(\mu_{w^-}, \sigma_{w^-})$. To get height values, the shape of the indentation is modeled by the cosine function $-\cos(x)$ for $x \in [-\pi/2, \pi/2]$ scaled to the width of the ring. Material depositions beside the indentation in form of rings having positive values. The width for the inner and outer rings are $w_k^{+i} \sim \mathcal{N}(\mu_{w^{+i}}, \sigma_{w^{+i}})$ and $w_k^{+o} \sim \mathcal{N}(\mu_{w^{+o}}, \sigma_{w^{+o}})$ and the height component is again modeled using the cosine function. All functions are combined to form the shape S_k of ring R_k (fig. 16).

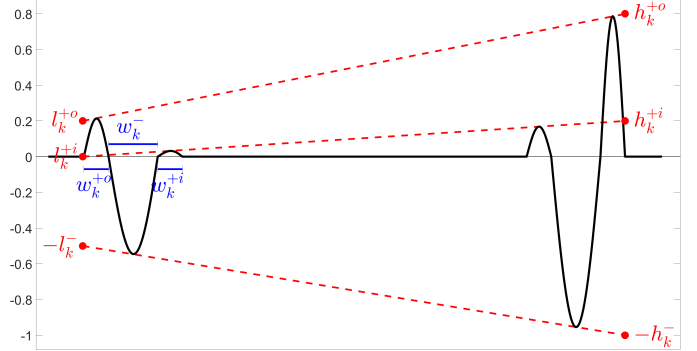
So far, perpendicularity between the milling head and the surface has been assumed. However, the milling head is often tilted forwards in direction of the tool movement to prevent re-cutting the surface. This direction is given by the angle $\phi_k \in (-\pi, \pi]$ in the x - y -plane between the tool path and the x -axis at point \tilde{c}_k . Tilting introduces a slope within the rings defined by the minimal $l_k^\bullet \sim \mathcal{N}(\mu_{l^\bullet}, \sigma_{l^\bullet})$ and maximal $h_k^\bullet \sim \mathcal{N}(\mu_{h^\bullet}, \sigma_{h^\bullet})$ indentation, inner and outer accumulation at the ring's front respectively back for $\bullet \in \{-, +i, +o\}$ (fig. 16). Since the tool's presence prevents pushing material to the inside, l^{+i} and h^{+i} are chosen small. Tilting T_k is then applied by multiplying with the shape S_k .

Finally, noise N_k is added, simulating irregularities caused by resistances in the material or vibrations during the process. It is modeled by a combination of $\lambda_k \sim \mathcal{P}(\lambda)$ sine curves with varying frequencies $\tau_{k_j} \sim \mathcal{P}(\tau)$ and random shifts $\xi_{k_j} \sim \mathcal{U}(-\pi, \pi)$ for $j = 1, \dots, \lambda_k$. Here, \mathcal{P} denotes a Poisson and \mathcal{U} a uniform distribution. Thus, $R_k = S_k \cdot T_k + N_k$ defines the sub-model for the appearance of one individual ring (fig. 16).

The third sub-model deals with the interaction of the neighboring rings. First, the rings are successively added into the model, according to their order by using a recursive function $f(R_1, \dots, R_k) = L_k \cdot R_k + (1 - L_k) \cdot f(R_1, \dots, R_{k-1})$ for $k = 1, \dots, n$ and $R_0 = 0$ (fig. 17). Since every part of the surface is processed several times, all associated rings must be taken into account with most of the weight on the temporally



(a) Sub-model for ring appearance using $\phi_k = 0$, from left to right: S_k, T_k, N_k, R_k .



(b) 1d intersection of $S_k \cdot T_k$.

Fig. 16: Illustration of sub-model for ring appearance with explanation of its parameters.

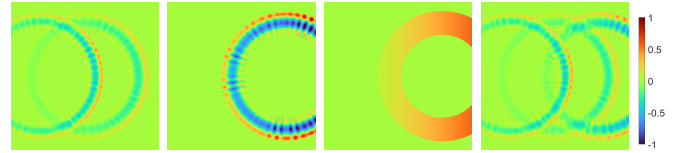


Fig. 17: Sub-model for rings' interaction using $\phi_k = 0$ (no tilting), from left to right: $f(R_1, R_2), R_3, L_3, f(R_1, R_2, R_3)$.

last ones. This is achieved by a convex combination. Weighting parameters are chosen as linear function $L_k : \mathbb{R}^2 \rightarrow [0, 1]$ which gives more weight to the front part of the ring than to the back. It is zero for points outside the ring. Values at the front and back of the rings are given by $a_k \sim \mathcal{U}(a^{\min}, a^{\max})$ and $b_k \sim \mathcal{U}(b^{\min}, b^{\max})$.

We refer to [87] for more details on the sub-models. A summary of the model parameters is given in table II. Some parameters are known explicitly (table I), while the others are estimated by visual comparison using high resolution topography measurements (fig. 9a). Simulations of the model using distinct parameter configurations are shown in fig. 18. Height values of the preliminary texture image \mathcal{T}_{pre} are adapted so that their distribution resembles that of the corresponding measurement \mathcal{M} . Mean values $\hat{\mu}_\bullet$ and sample variances $\hat{\sigma}_\bullet^2$, $\bullet \in \{\mathcal{M}, \mathcal{T}_{\text{pre}}\}$ are fit by setting $\mathcal{T} = \sqrt{\hat{\sigma}_{\mathcal{M}}/\hat{\sigma}_{\mathcal{T}_{\text{pre}}}} \cdot (\mathcal{T}_{\text{pre}} - \hat{\mu}_{\mathcal{M}}) + \hat{\mu}_{\mathcal{T}_{\text{pre}}}$.

VI. DEFECT MODELING

In this work we use the approach of Bosnar et al. [40] to generate multiple instances of defected object geometry, overview of which is provided in this chapter.

The defected object geometry is created through procedural geometry modeling of dents and scratches, thus ensuring correct light scattering. The three main steps are (1) generation of defect positions, (2) generation of 3D geometries representing

	Notation	Definition	Meaning	Distribution	Parameter	Values
Pattern	c_k	rings' center points	determined by tool path	$\mathcal{N}(\bar{c}_k, \Sigma_c)$	$\Sigma_c \in \mathbb{R}_{>0}^{2 \times 2}$	$(\Sigma_c)_{ii} = 0.01 \cdot \delta / \text{conf}$, $i = 1, 2$
	d	diameter of ring	diameter of milling head		$d \in \mathbb{R}_{>0}$	$d \in \{4, 8\}$ mm
	α	defines ρ (distance between neighboring tool paths)	amount of overlap of neighboring tool paths		$\alpha \in (0, 1)$	$\alpha \in \{0.2, 0.5, 0.8\}$
	γ	increase distance between neighboring tool paths	distance between blade and outer edge of tool		$\gamma \in (0, \alpha)$	$\gamma = 0.04$
	δ	distance between center points	depends on feed rate and tool's rotational speed		$\delta \in \mathbb{R}_{>0}$	$\delta = 0.09$ mm
	ϵ	amount of rings with changed order			$\epsilon \in [0, 1]$	$\epsilon = 0.01$
Appearance	w_k^-	width of indentation	width of cutting edge	$\mathcal{N}(\mu_{w^-}, \sigma_{w^-})$	$\mu_{w^-} \in (0, d/2)$ $\sigma_{w^-} \in \mathbb{R}_{>0}$	$\mu_{w^-} = 0.05$ mm $\sigma_{w^-} = 0.025 / \text{conf}$
	w_k^{+i}	width of inner accumulation	depends on edges' sharpness	$\mathcal{N}(\mu_{w^{+i}}, \sigma_{w^{+i}})$	$\mu_{w^{+i}} \in [0, d/2 - \mu_{w^-})$ $\sigma_{w^{+i}} \in \mathbb{R}_{>0}$	$\mu_{w^{+i}} = 0.025$ mm $\sigma_{w^{+i}} = 0.1 / \text{conf}$
	w_k^{+o}	width of outer accumulation	depends on edges' sharpness	$\mathcal{N}(\mu_{w^{+o}}, \sigma_{w^{+o}})$	$\mu_{w^{+o}} \in \mathbb{R}_{\geq 0}$ $\sigma_{w^{+o}} \in \mathbb{R}_{>0}$	$\mu_{w^{+o}} = 0.025$ mm $\sigma_{w^{+o}} = 0.1 / \text{conf}$
	ϕ_k	tilting direction	depends on tool path		$\phi_k \in (-\pi, \pi]$	computed by c_k
	l_k^-, h_k^-	minimal/maximal scaling of indentation depth	cutting depth with tilting	$\mathcal{N}(\mu_{\bullet^-}, \sigma_{\bullet^-})$	$\mu_{\bullet^-} \in \mathbb{R}_{\geq 0}$ $\sigma_{\bullet^-} \in \mathbb{R}_{>0}$	$\mu_{l^-} = 0.7$, $\mu_{h^-} = 1$ $\sigma_{\bullet^-} = 0.8 / \text{conf}$
	l_k^{+i}, h_k^{+i}	minimal/maximal scaling of inner accumulation height	depends on edges' sharpness	$\mathcal{N}(\mu_{\bullet^{+i}}, \sigma_{\bullet^{+i}})$	$\mu_{\bullet^{+i}} \in \mathbb{R}_{\geq 0}$ $\sigma_{\bullet^{+i}} \in \mathbb{R}_{>0}$	$\mu_{l^{+i}} = 0$, $\mu_{h^{+i}} = 0.2$ $\sigma_{\bullet^{+i}} = 0.5 / \text{conf}$
	l_k^{+o}, h_k^{+o}	minimal/maximal scaling of outer accumulation height	depends on edges' sharpness	$\mathcal{N}(\mu_{\bullet^{+o}}, \sigma_{\bullet^{+o}})$	$\mu_{\bullet^{+o}} \in \mathbb{R}_{\geq 0}$ $\sigma_{\bullet^{+o}} \in \mathbb{R}_{>0}$	$\mu_{l^{+o}} = 0.2$, $\mu_{h^{+o}} = 0.5$ $\sigma_{\bullet^{+o}} = 0.5 / \text{conf}$
	λ_k	number of sine curves		$\mathcal{P}(\lambda)$	$\lambda \in \mathbb{N}$	$\lambda = 50$
Interaction	τ_{k_j}	frequency of sine curves		$\mathcal{P}(\tau)$	$\tau \in \mathbb{N}$	$\tau = 50$
	ξ_{k_j}	shift of sine curves		$\mathcal{U}(-\pi, \pi)$		
	a_k	minimal value convex combination		$\mathcal{U}(a^{\min}, a^{\max})$	$a^{\min} \in [0, 1]$ $a^{\max} \in [a^{\min}, 1]$	$a^{\min} = 0$ $a^{\max} = 0.3$
b_k	maximal value convex combination		$\mathcal{U}(b^{\min}, b^{\max})$	$b^{\min} \in [0, 1]$ $b^{\max} \in [b^{\min}, 1]$	$b^{\min} = 0.1$ $b^{\max} = 0.4$	

TABLE II: Overview of all parameters needed for the milling model including their meaning and choices thereof. Choose $\text{conf} = 3$ for normally distributed parameters. Known parameters are highlighted (table I).

the defecting tools and (3) imprinting the defecting tools into the surface and creating geometrical masks which are used for generating defect annotations. Defect positions are determined by sampling points from an arbitrary distribution on the inspected product geometry. In this work we use normal distribution. The defects are embedded into the geometry using defecting tools, i.e. negatives of dents (denting tools) and scratches (scratch tools). Denting tools are typically spherical and parameterized for controlling their scale, rotation and shape. Scratch tools are created by performing a random walk on the product geometry, resulting in a path which is further converted into a solid geometry. Parameters are thickness and curviness, which control the size and shape of scratches.

The defecting tools are imprinted into the inspected product mesh using a Boolean difference operation. Geometrical masks, used for annotation generation (see section II-G) are then created using the inspected product mesh and the defecting tool. First, an intersection between the product mesh and the defecting tool mesh is computed. The resulting mesh represents a solid filling of the defect. The solid filling might be useful when the annotations must label missing area of the object. In this work we label only visible defected surface and therefore perform an additional step which results in mask shell. The defecting tool is first scaled with a factor in the range $[0.9, 1.0]$ and then intersected with the solid from the previous step.

The defect parameters can be chosen to match the shape,

size and positions of real defects observed in the measured defect topographies. However, more importantly, the parameter range can also be extended to produce defects beyond those observed in the available samples, i.e., rare occurrences or edge-cases. This enables creation of an arbitrary number of defected 3D objects containing a wide variety of possible defects (see fig. 19) for which pixel-precise annotations are generated.

VII. DUAL DATASET

Publicly available datasets for inspection of metal objects mostly focus on defect recognition over flat surfaces and single-view inspection setups [88]. With it, they reduce the expected appearance diversity of defects and surfaces in the image, making the defect recognition task easier. However, such restriction is not possible for inspection of more complex objects where multi-view imaging is required and visibility of the defects varies between different views. The aforementioned datasets contain objects such as hot rolled steel [89]–[92], slightly curved metal pads [93], [94], rails [95] and pipes [96]. Datasets of smaller metal objects with complex geometry are also present, however also under single-view inspection setups [97], [98]. Multi-view inspection setups inspect the same surface multiple times while varying at least the direction of the incoming light source or the direction of the camera to reduce the chance of missing defects due to low visibility. Examples in recent datasets include single-axis rotation [99], multiple illumination directions [100] and multiple view directions [42].

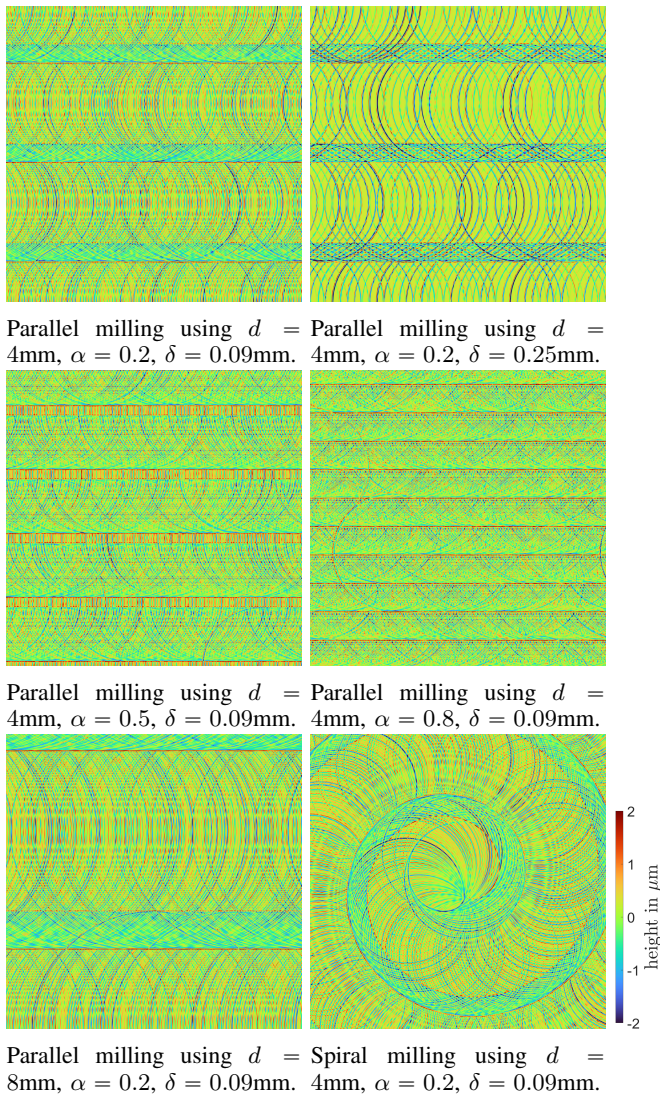


Fig. 18: Adapted simulated milled surfaces generated with different parameter configurations. Imaged region is $10\text{mm} \times 10\text{mm}$.

Synthetic datasets for inspection exist in form of generic stochastic textures [101], outdoor maintenance scenes [102], multi-object pose estimation task [29], industrial part recognition [103] and surface defect recognition [42].

We present a dual dataset consisting of a real and synthetic part, following the multi-view inspection setup described in [42]. Our dataset focuses on recognition difficulties arising from complex reflectance of different surface finish patterns which may cause defect curtaining.

A. Real Dataset

The real dataset was acquired using a setup consisting of a robot manipulator, a matrix grayscale camera, a diffuse ring light and an acquisition table. A thick black curtain removes any influence of the environment illumination or reflection from within the acquisition box. The manipulator is used to position the camera and illumination onto predefined viewpoints. The acquisition table is a flat surface covered in

diffuse black velvet and the acquired object is manually placed on top. The acquisition viewpoints are defined using V-POI [104] as an inspection plan, relative to the 3D model of the acquired object. Our acquisition plan consists of viewpoints focused on the middle of each inspected object face (faces A, B, and C), at angles 0, 10 and 20 degrees from the respective surface normal as visualized in fig. 20.

To minimize the placement error between the expected and actual position of the object, the operator must manually perform *object positioning*. This routine uses a predefined reference viewpoint - in our case the viewpoint perpendicular to the C-face - and a synthetic image of the object taken from it. The physical camera is placed into the position defined by the reference viewpoint and the reference synthetic image is overlaid. The object is then aligned manually to make the observed image match the reference image. For this procedure to be appropriate, either the synthetic image must contain image distortion introduced by the lens or the real image must be undistorted.

The real dataset consists of images of the test bodies defined in section III, acquired using the setup above and manually annotated using LabelMe [105]. The dataset contains 30 objects, 20 of which are defective, and 9 viewpoints per object. Overall this amounts to 270 annotated images, 180 of which display defects. The dataset was split into train-val-test sets. The test set contains the 10 non-defective objects and 10 defective objects. Train and validation sets contain the remaining 10 defective objects, where only 1 viewpoint per object is used for the validation set.

B. Synthetic dataset

The synthetic dataset generation environment described in section II was developed to match the physical acquisition setup. The dataset generator is an automated procedure which uses object, texture and defect specifications for generating annotated synthetic data in multiple stages. The first stage of the dataset generator is geometric defecting as described in section VI, which generates and applies defects to the original object geometry. We generate 30 defective synthetic object instances through stochastic sampling of defect locations and specifications defined in table III. The defect locations were sampled independently over the inspected surfaces using uniform barycentric face sampling. Finally, we group our generated defects into the classes 'dent' and 'scratch'.

The second stage produces texture images of the object surface using the methods introduced in section V. For each generated texture instance, the texture parameters are sampled at random from the values listed in table IV, thus producing controlled surface appearance variation. The ranges were chosen empirically by observing differences in physical samples and to model plausible variation in textures, such as milling at different translational speeds or amplitudes of parallel and orthogonal tool vibrations. For each of the three surface finishing methods, we generate 5 different texture instances.

The third stage combines the pre-generated synthetic objects and textures to produce annotated inspection images, as described in section II. A set of synthetic image-mask pairs are

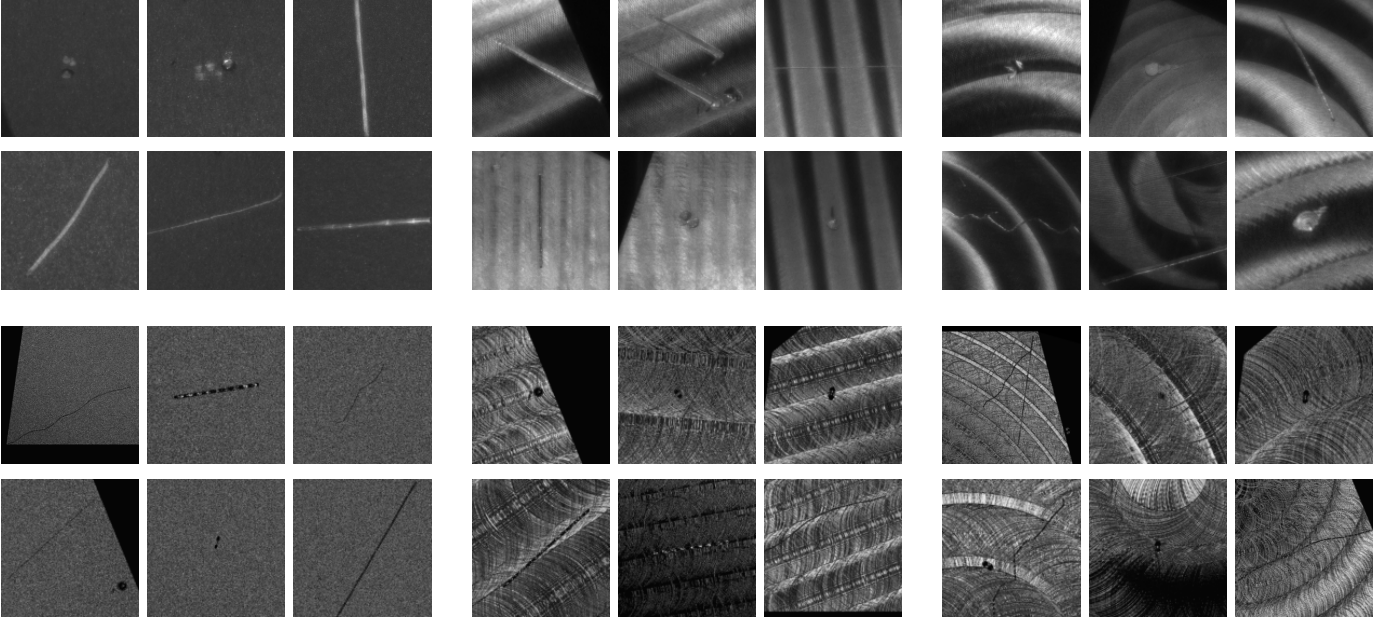


Fig. 19: Real (top) and synthetic (bottom) crops of defects on different surfaces. Left: sandblasted. Middle: parallel milling. Right: spiral milling.

Parameter	Small dent	Big dent	Flat scratch	Curvy scratch
Quantity	5	3	2	2
Diameter	[0.02, 0.2]	[0.2, 1.0]	[0.02, 0.2]	[0.02, 0.1]
Elongation	[1, 2]	[1, 4]	-	-
Depth	[0.05, 0.2]	[0.2, 1.0]	-	-
Path length	-	-	[5, 20]	[10, 20]
Step size	-	-	0.1	1.0

TABLE III: Defect quantities and specification ranges obtained from approximate measurements of their correspondents in physical samples, with gentle increase in ranges to model expected unobserved defects.

Parameter	Set of values
Ring center points noise (Σ_c)	{ 0.01 , 0.05, 0.1, 0.2, 0.4, 0.6, 0.8} $\cdot \delta/\text{conf}$
Ring distance (δ)	{0.7, 0.75, 0.8, 0.85, 0.9 , 0.95, 1.0, 1.05, 1.1}
Ring flip probability (ϵ)	{ 0.01 , 0.05, 0.1, 0.2, 0.3, 0.4, 0.5}
Ring width noise ($\sigma_{\omega-}$)	{0.015, 0.02, 0.025 , 0.03, 0.035} $\cdot 1/\text{conf}$
Ring depth noise (σ_{l-}, σ_{h-})	{0.4, 0.6, 0.8 , 1.0, 1.2} $\cdot 1/\text{conf}$
Cosine curves number (λ)	{30, 50 , 70}

TABLE IV: Texture parameter ranges used to modify the default values (highlighted) given in table II. The standard deviations were chosen by the 3σ rule such that the desired ranges of the random variables are obtained. Hence, we set $\text{conf} = 3$.

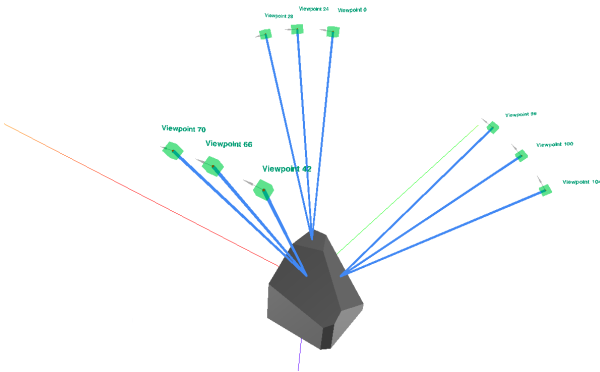


Fig. 20: Visualization of viewpoints used for inspection. The blue line shows the optical axis of the camera and has the length of focusing distance.

rendered for every synthetic object, following the same pre-defined inspection plan. Before rendering, each object surface gets assigned one of the pre-generated textures at random. Additionally, each time a texture is assigned it is randomly rotated by an angle in the range $[-15^\circ, 15^\circ]$ and translated by 5, 3 or 1 pixels for faces A, B and C, respectively. To model different surface oxidation levels, for each synthetic object we uniformly sample the material roughness parameter from the range $[0.05, 0.3]$. To produce a balanced dataset, we generate the same amount of image-mask pairs by re-using the correct object geometry instead of the defective ones.

Overall, the synthetic dataset consists of 30 correct and 30 defective object instances for each of the 10 physical objects. To remove the bias arising from the location and choice of defects when comparing results between textures, we re-use the same 30 defective object geometries across all of the physical objects. Each object is inspected using the same 9

viewpoints used in the pre-defined inspection plan, totaling in 5400 images, 2700 of which contain defects. The images were rendered using 256 SPP and 8 light bounces at the resolution 1224×1025 . The train-val-test set was produced ensuring label balance in the ratio 70 : 10 : 20 by splitting along the dimension of object instances.

A selection of images from our dataset is shown in fig. 21.

VIII. PIPELINE EVALUATION

To evaluate the quality of the pipeline we have to evaluate similarity of the data it produces to the real data acquired through inspection. Various metrics were proposed in recent works to estimate the quality of a dataset [106] through general dataset factors such as annotation consistency or class balance. However, these metrics usually provide limited insight into the data coverage of the dataset and ignore domain and task specific factors which could describe biases taken when collecting the dataset. Another approach of comparing the quality of synthetic datasets to the real ones is by measuring their utility for the given task through the model performance changes when using the synthetic data [12], [41], [42], [103], [107]–[109]. This however includes the inductive biases introduced by the model and training procedure selection making it more difficult to estimate the quality of the dataset itself. We thus perform a more direct comparison of datasets through image and data distribution similarity. When modeling a synthetic dataset, assumptions about the real world are made to increase the feasibility and economy of generating such datasets over the collection of more real data. To organize our evaluations, we propose a distinction between *a priori* quality, evaluating the accuracy of assumptions made before the data generation, and *a posteriori* quality, evaluating the accuracy of the generated synthetic data. To the best of the authors’ knowledge, this is a first evaluation of synthetic data quality which goes beyond the comparison of recognition model performances.

A. *A priori* quality

The *a priori* quality of a synthetic dataset quantifies the realism and precision of the environmental models used to generate the images compared to the target domain. It is reported through assumptions used to define parameters for the data generation and can be described prior to generating the final synthetic dataset. In our application, assumptions made to generate the dataset are tightly coupled to the physical processes used to manufacture and inspect the object. Using the same CAD model as used in manufacturing of the object, we guarantee the produced images will represent the correct geometry and restrict the data to the object of interest (section II-E). Using textures modeled to match the real surface measurements we restrict the recognition task to the nominal patterns present in the real objects (section V). Where possible, texture parameters are directly derived from processing parameters. All parameters are sampled around the nominal values to increase model robustness towards variations in the surface texture (section VII-B). Defect randomization contains ranges of parameters such as expected defect dimensions and shapes that cover defects present in the real objects, but also

defects outside the observed range for better generalization (section VII-B). By using physics based light simulation we ensure that the images are produced in a realistic way, holding the assumptions used for the material models and the rendering processes defined in section II-F. The simulated acquisition hardware (camera and light) uses the real acquisition hardware parameters to resemble the real inspection environment.

B. *A posteriori* quality

The *a posteriori* quality of a synthetic dataset describes the similarity of the generated data to the data collected in the target environment. This type of quality estimation relies on the established concepts of domain shifts actively used for methods of domain adaptation [110]. We categorize these qualities into domain similarity and task similarity.

Domain similarity measures the similarity between the distributions of real and synthetic images to quantify the covariate shift. In our case we measure the distance between generated images and the collected real images acquired using different types of metrics.

Value-wise metrics compare the global distributions of intensities between images. Distributions of image intensities can be summarized using histograms and compared using a suitable metric [111].

Pattern-wise similarity compares the local patterns between the images. This type of comparison is affected by the scene structures, e.g. patterns of the surface finish, the light source shape and the material reflectance function. Handcrafted image descriptors can be used to measure similarity of specific aspects of patterns in images, such as: pixel-wise closeness and alignment (e.g. mean absolute error, root mean squared error, cosine similarity) or statistical local similarity (e.g. SSIM [112], peak signal-to-noise ratio, Adapted Rand [113], GLCM [114]). Learned feature extractors alleviate the need to manually select specific features in images and instead rely on a very diverse dataset and deep learning to train a general purpose feature-space for pattern and shape comparison (e.g. LPIPS [115], FID [116]). However, due to inherent differences between natural (e.g. dogs, traffic, people) and technical images (e.g. surface inspection, manufacturing line, product appearance), the generality is still bounded to imaging context. To expand that context, one would need a large amount of representative technical images, which is not publicly available.

We evaluate the following metrics: Wasserstein distance between image histograms (HistWD), the mean absolute error (MAE), SSIM, and LPIPS using ImageNet pretrained AlexNet [117]. We limited our study to a single representative metric from each aforementioned subgroup with regards to their popularity in image quality estimation, interpretability and implementation availability. Our experiments will prove sufficient to discuss the influence and shortcomings of different metrics (section IX-B). To make the results easier to read, the metrics were normalized to the range $[0, 1]$ and flipped when necessary to report the degree of similarity (see table V). Our reasoning is that metrics which report the highest differences in the dataset (excluding trivial metrics) account best for small variations between the images in our datasets.

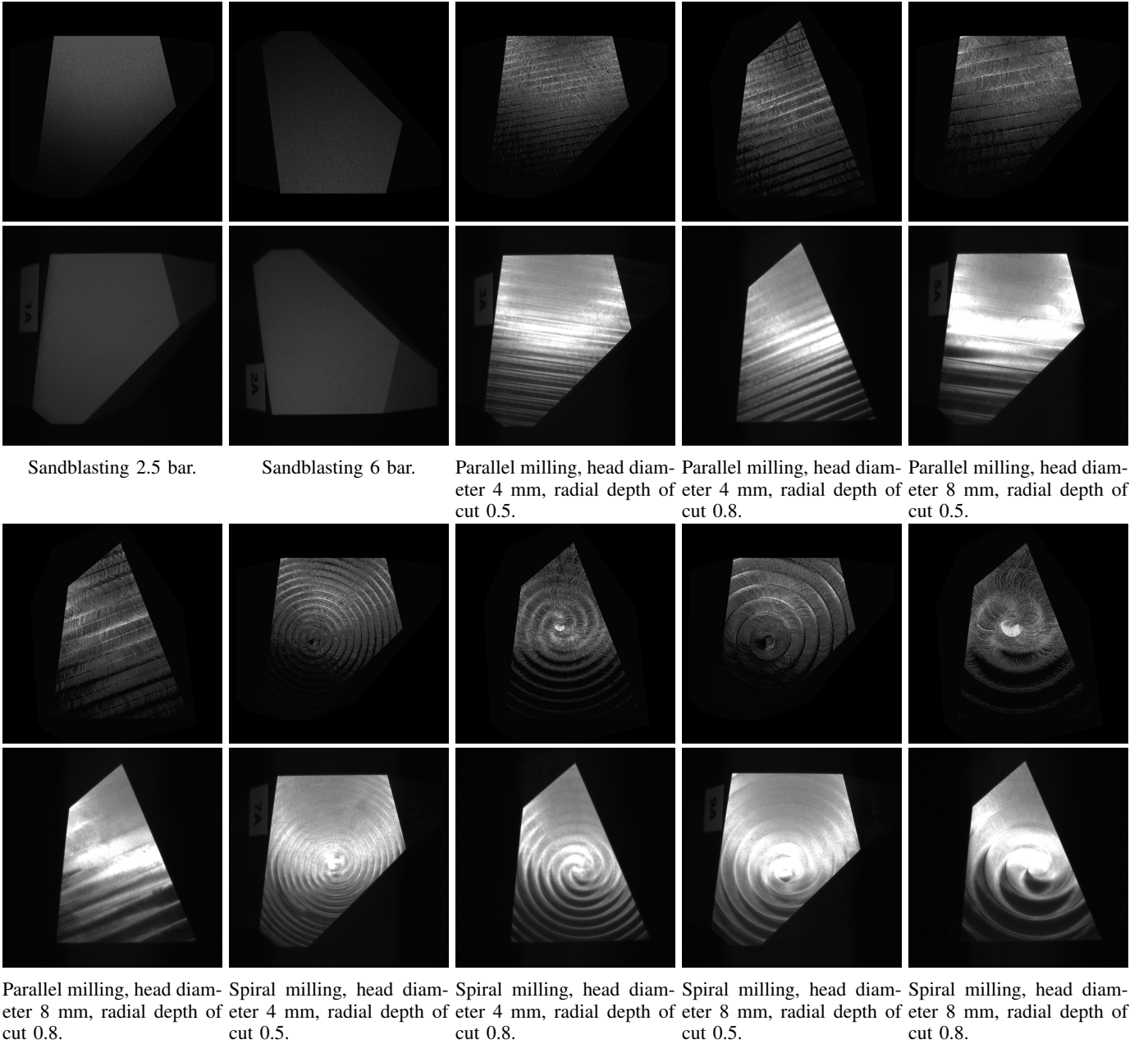


Fig. 21: Non-defective samples from the dual dataset. First and third row: synthesized images. Second and fourth row: real images of the same faces. The viewpoint is the 20-degree angle from a perpendicular view.

To compare our synthetic images to real ones we need to remove the influence of background noise and minor offsets, present from the imprecision of the acquisition system and background scene structures. We first mask out all the regions that do not contain the observed object face, thus removing the influence of sharp edges between the dark background and the object. For each viewpoint we construct a common meta-mask from the intersection of face masks corresponding to that viewpoint. To reduce the difference in intensity levels, we manually estimate parameters of a linear transformation to bring the histograms between matching real and synthetic images closer together. The minimal grey value in real images is typically larger than 0 while synthetic images also show

grey values down to 0. Thus, for each texture type, we add the mean minimal grey value observed in the real images to all synthetic images.

Next, we estimate a multiplication factor that jointly compensates for the illumination intensity and material absorption difference between synthetic and real data. This method is justified because the factor can be extracted from the integral of the rendering equation [46], assuming that the inter-reflectance of the surface meso-structures is negligible. The assumption holds for our case since we use normal-mapping for meso-structure, which does not produce inter-reflectance. The bias value is added to all of the pixels to compensate for the ambient illumination caused by the low-intensity inter-reflections

Method	Sandblasted	Parallel	Spiral	All
1-HistWD	0.980	0.932	0.942	0.946
1-MAE	0.807	0.681	0.655	0.696
SSIM	0.896	0.561	0.585	0.638
1-LPIPS	0.916	0.660	0.686	0.722

TABLE V: Domain similarities averaged within and across texture types, bounded to interval $[0, 1]$. Histogram WD, MAE and LPIPS were inverted to be interpreted as the degree of similarity.

of the inspected object and the inspection environment. It can be observed in the image histograms as a gap of zeros between the illumination value 0 and the first next intensity value in the histogram. We estimate the bias by calculating the average gap size. The estimated factors and biases are: (0.632, 34) for sandblasted, (1.481, 39) for parallel and (1.526, 33) for spiral milling. Finally, since the synthetic pinhole camera model does not include blurring and imperfections of the real camera, we artificially blur the synthetic images using defocus blur [118] with radius 1.0.

The synthetic data does not model an exact 1:1 replica of the texture found on a single real object, but stochastically varying texture appearance. Therefore, we measure the distance to the closest synthetic sample, similarly to a one-sided Chamfer distance. When evaluating the metrics, for each viewpoint we evaluate the metric between the real image and all available synthetic object instances and select the value representing the highest similarity (lowest distance). In table V for each texture type we report the metric value averaged across all viewpoints and objects sharing the same texture type.

Task similarity is affected by concept shift and estimates how well the task function, mapping inputs to labels, obtained on synthetic data transfers to the target dataset. In our case we measure how well an image semantic segmentation model trained on synthetic data generalizes to the real data. In the field of domain adaptation [110], a common approach is to report the difference in task metrics. As discussed in [119], this approach measures the difference in biases present in the two datasets, which can be interpreted as domain shifts when working with datasets acquired from different environments.

We train a UNet [120] with a ResNet-50 [121] backbone from 5 random parameter initializations per experiment and report the top obtained result, to reduce the bias of weight initialization. The model is trained to perform semantic segmentation through pixel classification into the classes background, dent, and scratch. Since the non-background classes are highly underrepresented, we observed the need to use class weighting which we empirically found to be (1, 1.5, 1.5) for the real and (1, 2, 2) for the synthetic dataset. We optimize the models using the AdamW optimizer [122] with learning rate 10^{-4} and L_2 weight regularization of 10^{-5} , for a maximum of 1000 epochs with early stopping at validation loss convergence upon 5 consecutive validations without at least 10^{-2} relative improvement. For model fine-tuning we use the learning rate 10^{-5} . For memory efficiency, during training we extract random image crops of size 256×256 and during evaluation we split the images into a 3×3 grid of patches of size 416×352 . All images were zero padded to ensure dimension

divisibility correctness when evaluating the UNet and image patching. To speed up model training, we center the images linearly between $[-1, 1]$.

Since rendering images is a memory and compute expensive operation we offload as much of the domain alignment as possible to online post-processing. To simulate the non-zero background, we artificially add Gaussian noise of amplitudes in the interval $[0, 5]$ to the background around the object. To simulate the vertical blooming effect caused by photon leakage within the saturated regions of the CCD sensor array, we extract the maximum value of each image column, mask the column using a threshold 0.95, blur it using a box filter of size 64, multiply by 0.02 and add it to the original image with clipping. Manually annotated real images contain imprecision in masks as they often cover the area around the rim of the defect. We emulate this by dilating the synthetic masks by 1 pixel. The synthetic images contain masks in regions that have mostly uniform value and should be considered invisible. We pre-filter the masks to remove defects with insufficient visibility. We empirically estimate the visibility as the difference between the mean intensity of the defect and the mean intensity of the surface ring around the defect, calculated as difference between the defect mask which is dilated 2 times and the original defect mask. Defects are considered visible if the difference in means is over 0.05.

Data augmentation further increases the diversity of the dataset and helps regularizing the recognition model to consider the important features. To simulate the offsets of the camera we use random rotation of amplitude 15° . Illumination strength and object material diffusion variation can be jointly controlled using random exposure from the interval $[-0.5, 1.5]$. To simulate the blurred background structures and impurities in the lens or the light carrying medium, we add Gaussian noise of amplitude in the range $[0, 5]$ to the entire image and then blur it using defocus blur [118] of kernel sizes in the interval $[1, 3]$. Gaussian noise of amplitude in $[0, 5]$ is added once more to simulate the static noise of the real images. Finally, images can be randomly flipped horizontally to increase the texture-structure pair diversity. All of the augmentations are performed with probability of 50%. Finally, we perform intensity biased random cropping [42] using threshold 15 to ensure production of crops that contain more visible structures in the image.

The results of image segmentation are collected in table VI. When computing the mean score, the contribution of the background class to the mean value was ignored as it is the majority class that would skew the results away from the defect classes. To evaluate the concept shift, we compare common semantic segmentation metrics of the model generalization when trained on the real subset to the synthetic subset.

IX. DISCUSSION

A. Pipeline controllability and simplicity

The pipeline is very versatile and allows generation of a wide variety of texture variations needed for domain randomization. Parametrization of the modules allows defining elements using physical measurements. The modularity of the

Texture	Domains	mP	mR	mF1	mIoU
Sandblasted	Sy \rightarrow Sy	57.0	53.1	54.7	37.7
	Sy \rightarrow Re	34.0	64.3	41.7	26.3
	Sy+ft \rightarrow Re	60.1	71.9	65.5	49.6
	Re \rightarrow Re	57.9	61.9	59.1	42.6
Parallel	Sy \rightarrow Sy	57.1	39.6	45.6	29.6
	Sy \rightarrow Re	26.5	23.0	23.5	13.8
	Sy+ft \rightarrow Re	52.6	33.4	38.3	23.9
	Re \rightarrow Re	50.3	34.5	40.8	25.8
Spiral	Sy \rightarrow Sy	59.5	39.7	47.6	31.3
	Sy \rightarrow Re	35.2	22.1	26.4	15.5
	Sy+ft \rightarrow Re	49.5	40.1	43.9	28.4
	Re \rightarrow Re	50.6	43.1	46.2	30.7
All	Sy \rightarrow Sy	59.4	46.0	51.5	34.7
	Sy \rightarrow Re	32.2	31.3	31.6	18.9
	Sy+ft \rightarrow Re	59.0	49.1	53.1	36.1
	Re \rightarrow Re	59.0	48.2	52.6	35.8

TABLE VI: Task similarities between texture groups. The domains represent the experiment *training* \rightarrow *testing* domains, with the real (Re) and synthetic (Sy) domains. Fine-tuning (ft) is performed using real data after training on synthetic data.

generation process allows fast iterations during initial dataset development phases and extensibility to new textures and defects. The rendering is the most computationally demanding component, but it can be easily parallelized.

The large number of parameters make it difficult to study the influence of different parameter sampling schemes on the recognition performance. However, this pipeline opens the opportunity to design a higher level of abstraction for dataset design through modeling of lower dimensional constraints over larger sets of parameters. While this study is out of scope of this paper, we strongly encourage it to be performed in the future.

B. Domain similarity

Measuring texture similarity is a difficult problem due to surface and acquisition imperfections present in the real data. Camera blurring, surface imperfections and other effects move away from the nominal texture without degrading its performance, thus producing falsely bad results. In addition, it is difficult to generate a nominal image that perfectly aligns to the acquired image due camera-object and texture-object alignments. In this work we instead rely on methods that compare global or local pixel statistics of textures to remove alignment. From results in table V we observe that the sandblasted textures have the highest degree of similarity compared to the parallel and spiral milling textures. This result is related to the simplicity of modeling the sandblasted texture as the texture appears as mostly uniform noise. More structured textures such as those of milling are more difficult to replicate as they have significantly more parameters that interplay to produce unique patterns.

Comparing the values of metrics is difficult, even though they are bounded between $[0, 1]$ and might measure similar properties of images, they do not share the same linearity of response to changes in inputs. A separate study is required to compare which physical properties different metrics attempt

measuring over additional datasets. Since such a study targets a different task, it requires different definitions of dataset parameters which is out of scope of this study.

C. Task similarity and recognition performance

The defect recognition results in table VI show very similar performance in all experiments, except when the model trained on the synthetic domain is evaluated directly on the real domain. The similarity of results, even after fine-tuning, indicates that the models are saturated in their capacity to solve the task. The low generalization to the real domain indicates that there exists a misalignment between the synthetic and real data distributions, both in the form of covariate shift (as observed by similarity metrics) and concept shift. Results of models trained on all textures do not surpass the performance on the highest performing, sandblasted texture, leading us to the conclusion that training a model on multiple textures at once does not give any benefit over training a separate model for each texture.

When inspecting the model predictions over the datasets we notice some patterns. All models tend to predict masks that are slightly wider than the label. Most false positives come from the milled textures, in the lines where two milling path circles overlap and along the exit lines. In sandblasted textures, tiny glints from the surface are often falsely predicted as defected. False positives are also present in minor deviations in object shape such as edge scuffing, beveling, deeper sandblasting holes, etched signature, on paper label sticker and where the milled pattern has high contrast. Models also tend to predict defects on out-of-focus faces that the annotator left as unannotated due to heavy blurring or unrecognizability. When predicting scratches, the models prefer areas where the texture has lower contrast and defect stand out. Some scratches that are not close to being horizontal or vertical are not predicted, even though the visibility is similar to the predicted ones, meaning the recognition models need more filters in lower levels or more explicit rotation invariance. Overall, it seems a higher resolution might help the model distinguish between defect and texture patterns.

D. Influence of domain similarity on task performance

The largest drop in recognition performance is on milled textures, which is consistent with their lower domain similarity compared to sandblasted textures. Furthermore, SSIM and LPIPS seem to be linearly correlated to the best obtained recognition performance. If this were true, we could use these metrics when iteratively improving the synthetic data to reduce the domain gap at its source, the data simulation or generation process. This forms the questions of whether these metrics are indeed predictive of the domain gap that impedes the recognition performance, which other metrics have a similar property and why MAE and histogram comparison do not seem to be. These questions are vastly out of scope of this paper and we leave their treatment for a future study.

X. CONCLUSION

This work presents a rule-based solution for generating synthetic data of various surface finishes for metal objects.

The solution consists of surface texture models controlled by parameters measured in examples, application of specification based defects and rendering to produce a synthetic images and pixel-wise annotations. An approach for synthetic image and distribution quality estimation is proposed. Utility of generated data is measured on the defect segmentation task. Results of quality estimation shows correlation to results of the segmentation task. The utility of the synthetic data requires further research due to the need for modeling of significant imperfections in the image acquisition system and object geometry.

ACKNOWLEDGMENTS

This work was funded by the German Federal Ministry of Education and Research (BMBF) [grant number 01IS21058 (SynosIs)].

REFERENCES

- [1] P. Gospodnetić, D. Mosbach, M. Rauhut, and H. Hagen, "Flexible surface inspection planning pipeline," in *6th International Conference on Control, Automation and Robotics (ICCAR)*, pp. 644–652, 2020.
- [2] M. Wagenstetter, P. Gospodnetic, L. Bosnar, J. Fulir, D. Kreul, H. Rushmeier, T. Aicher, A. Hellmich, and S. Ihlenfeldt, "Synthetically generated images for industrial anomaly detection," in *Proceedings of IEEE International Conference on Emerging Technologies and Factory Automation*, 2024.
- [3] S. I. Nikolenko, *Synthetic data for deep learning*, vol. 174. Springer, 2021.
- [4] M. Haselmann and D. P. Gruber, "Pixel-wise defect detection by cnns without manually labeled training data," *Applied Artificial Intelligence*, vol. 33, no. 6, pp. 548–566, 2019.
- [5] K. Schladitz, C. Redenbach, T. Barisin, C. Jung, N. Jeziorski, L. Bosnar, J. Fulir, and P. Gospodnetic, "Simulation of microstructures and machine learning," in *CMDSD14*, (Paris), Springer Proceedings in Mathematics and Statistics, 2023.
- [6] S. Jain, G. Seth, A. Paruthi, U. Soni, and G. Kumar, "Synthetic data augmentation for surface defect detection and classification using deep learning," *J. Intell. Manuf.*, vol. 33, p. 1007–1020, apr 2020.
- [7] G. Zhang, K. Cui, T.-Y. Hung, and S. Lu, "Defect-gan: High-fidelity defect synthesis for automated defect inspection," in *IEEE WACV*, pp. 2523–2533, 2021.
- [8] R. Wang, S. Hoppe, E. Monari, and M. Huber, "Defect transfer gan: Diverse defect synthesis for data augmentation," in *33rd British Machine Vision Conference 2022, BMVC 2022, London, UK, November 21-24, 2022*, BMVA Press, 2022.
- [9] J. Wei, F. Shen, C. Lv, Z. Zhang, F. Zhang, and H. Yang, "Diversified and multi-class controllable industrial defect synthesis for data augmentation and transfer," in *2023 IEEE/CVF CVPRW*, pp. 4445–4453, 2023.
- [10] O. Schmedemann, S. Schlodinski, D. Holst, and T. Schüppstuhl, "Adapting synthetic training data in deep learning-based visual surface inspection to improve transferability of simulations to real-world environments," in *Automated Visual Inspection and Machine Vision V*, vol. 12623, pp. 25–35, SPIE, 2023.
- [11] T. Dahmen, P. Trampert, F. Boughorbel, J. Sprenger, M. Klusch, K. Fischer, C. Kübel, and P. Slusallek, "Digital reality: a model-based approach to supervised learning from synthetic data," *AI Perspectives*, vol. 1, no. 1, p. Article No.2, 2019. 43.22.02; LK 01.
- [12] A. Tsirikoglou, G. Eilertsen, and J. Unger, "A Survey of Image Synthesis Methods for Visual Machine Learning," *Computer Graphics Forum*, 2020.
- [13] G. Varol, J. Romero, X. Martin, N. Mahmood, M. J. Black, I. Laptev, and C. Schmid, "Learning from synthetic humans," in *Proceedings of the IEEE conference on computer vision and pattern recognition*, pp. 109–117, 2017.
- [14] D. Park and D. Ramanan, "Articulated pose estimation with tiny synthetic videos," in *Proceedings of the IEEE Conference on Computer Vision and Pattern Recognition Workshops*, pp. 58–66, 2015.
- [15] M. Fabbri, F. Lanzi, S. Calderara, A. Palazzi, R. Vezzani, and R. Cucchiara, "Learning to detect and track visible and occluded body joints in a virtual world," in *Proceedings of the European conference on computer vision (ECCV)*, pp. 430–446, 2018.
- [16] A. Kortylewski, A. Schneider, T. Gerig, B. Egger, A. Morel-Forster, and T. Vetter, "Training deep face recognition systems with synthetic data," *arXiv preprint arXiv:1802.05891*, 2018.
- [17] A. Dosovitskiy, G. Ros, F. Codevilla, A. Lopez, and V. Koltun, "Carla: An open urban driving simulator," in *Conference on robot learning*, pp. 1–16, PMLR, 2017.
- [18] A. Shafaei, J. J. Little, and M. Schmidt, "Play and learn: Using video games to train computer vision models," *arXiv preprint arXiv:1608.01745*, 2016.
- [19] B. Hurl, K. Czarnecki, and S. Waslander, "Precise synthetic image and lidar (presil) dataset for autonomous vehicle perception," in *2019 IEEE Intelligent Vehicles Symposium (IV)*, pp. 2522–2529, IEEE, 2019.
- [20] J. Tremblay, T. To, B. Sundaralingam, Y. Xiang, D. Fox, and S. Birchfield, "Deep object pose estimation for semantic robotic grasping of household objects," *arXiv preprint arXiv:1809.10790*, 2018.
- [21] "Nvidia isaac - the accelerated platform for robotics and ai." <https://www.nvidia.com/en-us/deep-learning-ai/industries/robotics/>. Accessed: 2023-01-30.
- [22] S. Khan, B. Phan, R. Salay, and K. Czarnecki, "Procsy: Procedural synthetic dataset generation towards influence factor studies of semantic segmentation networks," in *CVPR workshops*, vol. 3, p. 4, 2019.
- [23] E. Buls, R. Kadikis, R. Cacurs, and J. Arents, "Generation of synthetic training data for object detection in piles," in *Eleventh International Conference on Machine Vision (ICMV 2018)*, vol. 11041, pp. 533–540, SPIE, 2019.
- [24] K. Greff, F. Belletti, L. Beyer, C. Doersch, Y. Du, D. Duckworth, D. J. Fleet, D. Gnanaprasam, F. Golemo, C. Herrmann, *et al.*, "Kubric: A scalable dataset generator," in *Proceedings of the IEEE/CVF Conference on Computer Vision and Pattern Recognition*, pp. 3749–3761, 2022.
- [25] S. Moonen, B. Vanherle, J. de Hoog, T. Bourgana, A. Bey-Temsamani, and N. Michiels, "Cad2render: A modular toolkit for gpu-accelerated photorealistic synthetic data generation for the manufacturing industry," in *Proceedings of the IEEE/CVF Winter Conference on Applications of Computer Vision*, pp. 583–592, 2023.
- [26] M. Wieler and T. Hahn, "Weakly supervised learning for industrial optical inspection," in *DAGM symposium in*, vol. 6, 2007.
- [27] T. Bao, J. Chen, W. Li, X. Wang, J. Fei, L. Wu, R. Zhao, and Y. Zheng, "Miad: A maintenance inspection dataset for unsupervised anomaly detection," in *Proceedings of the IEEE/CVF International Conference on Computer Vision*, pp. 993–1002, 2023.
- [28] A. Boikov, V. Payor, R. Savelev, and A. Kolesnikov, "Synthetic data generation for steel defect detection and classification using deep learning," *Symmetry*, vol. 13, no. 7, p. 1176, 2021.
- [29] P. De Roovere, S. Moonen, N. Michiels, and F. Wyffels, "Dataset of industrial metal objects," 2022.
- [30] J. de Hoog, G. Grimard, T. Bourgana, N. Michiels, S. Moonen, R. De Geest, and A. Bey-Temsamani, "Cad2x - a complete, end-to-end solution for training deep learning networks for industrial applications," in *2023 Smart Systems Integration Conference and Exhibition (SSI)*, pp. 1–7, 2023.
- [31] F. A. Saiz, G. Alfaro, I. Barandiaran, S. Garcia, M. Carretero, and M. Graña, "Synthetic data set generation for the evaluation of image acquisition strategies applied to deep learning based industrial component inspection systems," in *CEIG*, pp. 1–8, 2021.
- [32] B. Yang, Z. Liu, G. Duan, and J. Tan, "Mask2defect: A prior knowledge-based data augmentation method for metal surface defect inspection," *IEEE Transactions on Industrial Informatics*, vol. 18, no. 10, pp. 6743–6755, 2021.
- [33] A. G. Abubakr, I. Jovancevic, N. I. Mokhtari, H. B. Abdallah, and J.-J. Orteu, "On learning deep domain-invariant features from 2d synthetic images for industrial visual inspection," in *Fifteenth International Conference on Quality Control by Artificial Vision*, vol. 11794, pp. 317–325, SPIE, 2021.
- [34] A. Kim, K. Lee, S. Lee, J. Song, S. Kwon, and S. Chung, "Synthetic data and computer-vision-based automated quality inspection system for reused scaffolding," *Applied Sciences*, vol. 12, no. 19, p. 10097, 2022.
- [35] S. Sauer, M. Borkar, D. Sasidharan, and T. Dunker, "Model-based visual inspection with machine learning methods using simulation of the expected camera view." Workshop on "Generating synthetic image data for AI" at the KI 2022 (virtual, hosted in Trier/Germany), September 2022.

- [36] B. Raymond, G. Guennebaud, and P. Barla, "Multi-scale rendering of scratched materials using a structured sv-brdf model," *ACM Transactions on Graphics (TOG)*, vol. 35, no. 4, pp. 1–11, 2016.
- [37] L. Bosnar, D. Saric, S. Dutta, T. Weibel, M. Rauhut, H. Hagen, and P. Gospodnetic, "Image synthesis pipeline for surface inspection," *LEVIA 20: Leipzig Symposium on Visualization in Applications.*, 2020.
- [38] P. Gospodnetic, *Visual Surface Inspection Planning for Industrial Applications*. Fraunhofer Verlag, 2021.
- [39] L. Bosnar, M. Rauhut, H. Hagen, and P. Gospodnetic, "Texture synthesis for surface inspection," *LEVIA 22: Leipzig Symposium on Visualization in Applications.*, 2022.
- [40] L. Bosnar, H. Hagen, and P. Gospodnetic, "Procedural defect modeling for virtual surface inspection environments," *IEEE Computer Graphics and Applications*, 2023.
- [41] O. Schmedemann, M. Baaß, D. Schoepflin, and T. Schüppstuhl, "Procedural synthetic training data generation for ai-based defect detection in industrial surface inspection," *Procedia CIRP*, vol. 107, pp. 1101–1106, 2022.
- [42] J. Fulir, L. Bosnar, H. Hagen, and P. Gospodnetić, "Synthetic data for defect segmentation on complex metal surfaces," in *2023 IEEE/CVF Conference on Computer Vision and Pattern Recognition Workshops (CVPRW)*, pp. 4423–4433, 2023.
- [43] J. Dorsey, H. Rushmeier, and F. Sillion, *Digital modeling of material appearance*. Elsevier, 2010.
- [44] C. Shannon, "Communication in the presence of noise," *Proceedings of the IRE*, vol. 37, pp. 10–21, jan 1949.
- [45] D. P. Greenberg, K. E. Torrance, P. Shirley, J. Arvo, E. Lafortune, J. A. Ferwerda, B. Walter, B. Trumbore, S. Pattanaik, and S.-C. Foo, "A framework for realistic image synthesis," in *Proceedings of the 24th annual conference on Computer graphics and interactive techniques*, pp. 477–494, 1997.
- [46] J. T. Kajiya, "The rendering equation," in *Proceedings of the 13th annual conference on Computer graphics and interactive techniques*, pp. 143–150, 1986.
- [47] M. Pharr, W. Jakob, and G. Humphreys, *Physically based rendering: From theory to implementation*. Morgan Kaufmann, 2016.
- [48] F. Beauce, E. Tovagliari, and contributors, "appleseed," Sept. 2019.
- [49] B. Walter, S. R. Marschner, H. Li, and K. E. Torrance, "Microfacet models for refraction through rough surfaces.," *Rendering techniques*, vol. 2007, p. 18th, 2007.
- [50] C. Kulla and A. Conty, "Revisiting physically based shading at image-works," *SIGGRAPH Course, Physically Based Shading*, vol. 2, no. 3, 2017.
- [51] E. Turquin, "Practical multiple scattering compensation for microfacet models," URL: https://blog.selfshadow.com/publications/turquin/ms_comp_final.pdf, vol. 45, no. 3, 2019.
- [52] M. S. Mikkelsen, "Bump mapping unparametrized surfaces on the gpu," *Journal of graphics, gpu, and game tools*, vol. 15, no. 1, pp. 49–61, 2010.
- [53] P. Guerrero, M. Hašan, K. Sunkavalli, R. Měch, T. Boubekeur, and N. J. Mitra, "Matformer: A generative model for procedural materials," *arXiv preprint arXiv:2207.01044*, 2022.
- [54] "Adobe substance 3d assets." <https://substance3d.adobe.com/assets>. Accessed: 2023-01-30.
- [55] D. S. Ebert, F. K. Musgrave, D. Peachey, K. Perlin, and S. Worley, *Texturing & modeling: a procedural approach*. Morgan Kaufmann, 2003.
- [56] Z. Dong, B. Walter, S. Marschner, and D. P. Greenberg, "Predicting appearance from measured microgeometry of metal surfaces," *ACM Transactions on Graphics (TOG)*, vol. 35, no. 1, pp. 1–13, 2015.
- [57] L. Bosnar, H. Hagen, and P. Gospodnetic, "Texture synthesis for automated visual surface inspection planning," tech. rep., Fraunhofer ITWM, 2021.
- [58] K. Hormann, B. Lévy, and A. Sheffer, "Mesh parameterization: Theory and practice," in *ACM SIGGRAPH 2007 Courses*, SIGGRAPH '07, (New York, NY, USA), p. 1–es, Association for Computing Machinery, 2007.
- [59] P. G. Vivo and J. Lowe, "The book of shaders," *Dosegljivo: https://thebookofshaders.com*, 2015.
- [60] J. Dong, J. Liu, K. Yao, M. Chantler, L. Qi, H. Yu, and M. Jian, "Survey of procedural methods for two-dimensional texture generation," *Sensors*, vol. 20, no. 4, p. 1135, 2020.
- [61] S. Deguy, "The new age of procedural texturing.," 2019.
- [62] C. Dostal and K. Yamafune, "Photogrammetric texture mapping: A method for increasing the fidelity of 3d models of cultural heritage materials," *Journal of Archaeological Science: Reports*, vol. 18, pp. 430–436, 2018.
- [63] M. Ritz, S. Breitfelder, P. Santos, A. Kuijper, and D. W. Fellner, "Seamless and non-repetitive 4d texture variation synthesis and real-time rendering for measured optical material behavior," *Computational Visual Media*, vol. 5, pp. 161–170, 2019.
- [64] N. Jetchev, U. Bergmann, and R. Vollgraf, "Texture synthesis with spatial generative adversarial networks," *arXiv preprint arXiv:1611.08207*, 2016.
- [65] U. Bergmann, N. Jetchev, and R. Vollgraf, "Learning texture manifolds with the periodic spatial gan," *arXiv preprint arXiv:1705.06566*, 2017.
- [66] T. Zeltner, F. Rousselle, A. Weidlich, P. Clarberg, J. Novák, B. Bitterli, A. Evans, T. Davidovič, S. Kallweit, and A. Lefohn, "Real-time neural appearance models," *arXiv preprint arXiv:2305.02678*, 2023.
- [67] L. Raad, A. Davy, A. Desolneux, and J.-M. Morel, "A survey of exemplar-based texture synthesis," 2017.
- [68] B. Galerne, Y. Gousseau, and J.-M. Morel, "Random phase textures: Theory and synthesis," *IEEE Transactions on Image Processing*, vol. 20, no. 1, pp. 257–267, 2011.
- [69] D. Heeger and J. Bergen, "Pyramid-based texture analysis/synthesis," in *Proceedings., International Conference on Image Processing*, vol. 3, pp. 648–651 vol.3, 1995.
- [70] T. Briand, J. Vacher, B. Galerne, and J. Rabin, "The Heeger & Bergen Pyramid Based Texture Synthesis Algorithm," *Image Processing On Line*, vol. 4, pp. 276–299, 2014. <https://doi.org/10.5201/ipol.2014.79>.
- [71] J. Portilla and E. Simoncelli, "A parametric texture model based on joint statistics of complex wavelet coefficients," *International Journal of Computer Vision*, vol. 40, 10 2000.
- [72] J. Vacher and T. Briand, "The portilla-simoncelli texture model: towards understanding the early visual cortex," *Image Processing On Line*, vol. 11, pp. 170–211, 2021. <https://doi.org/10.5201/ipol.2021.324>.
- [73] A. Efros and W. Freeman, "Image quilting for texture synthesis and transfer," *Computer Graphics (Proc. SIGGRAPH'01)*, vol. 35, 07 2001.
- [74] L. Raad and B. Galerne, "Efros and Freeman Image Quilting Algorithm for Texture Synthesis," *Image Processing On Line*, vol. 7, pp. 1–22, 2017. <https://doi.org/10.5201/ipol.2017.171>.
- [75] A. A. Efros and T. K. Leung, "Texture synthesis by non-parametric sampling," in *Proceedings of the Seventh IEEE International Conference on Computer Vision*, vol. 2, pp. 1033–1038, 1999.
- [76] P. Guehl, R. Allègre, J.-M. Dischler, B. Benes, and E. Galin, "Semi-procedural textures using point process texture basis functions," *Computer Graphics Forum*, vol. 39, no. 4, pp. 159–171, 2020.
- [77] Y. Hu, C. He, V. Deschaintre, J. Dorsey, and H. Rushmeier, "An inverse procedural modeling pipeline for svbrdf maps," *ACM Transactions on Graphics (TOG)*, vol. 41, no. 2, pp. 1–17, 2022.
- [78] J. Zhu, S. Zhao, Y. Xu, X. Meng, L. Wang, and L.-Q. Yan, "Recent advances in glinty appearance rendering," *Computational Visual Media*, vol. 8, no. 4, pp. 535–552, 2022.
- [79] X. Cherman, F. Claux, and S. Mérrillou, "Glint rendering based on a multiple-scattering patch brdf," *Computer Graphics Forum*, vol. 38, no. 4, pp. 27–37, 2019.
- [80] M. P. Groover, *Fundamentals of modern manufacturing: materials, processes, and systems*. John Wiley & Sons, 2020.
- [81] T. H. Childs, K. Maekawa, T. Obikawa, and Y. Yamane, *Metal machining: theory and applications*. Butterworth-Heinemann, 2000.
- [82] C. Felhő, B. Karpuschewski, and J. Kundrák, "Surface roughness modelling in face milling," *Procedia CIRP*, vol. 31, pp. 136–141, 2015.
- [83] C. Felhő and J. Kundrák, "Effects of setting errors (insert run-outs) on surface roughness in face milling when using circular inserts," *Machines*, vol. 6, no. 2, 2018.
- [84] J. Kundrák, C. Felhő, and A. Nagy, "Analysis and prediction of roughness of face milled surfaces using cad model," *Manufacturing Technology*, vol. 22, pp. 558–572, 2022.
- [85] M. Hadad and M. Ramezani, "Modeling and analysis of a novel approach in machining and structuring of flat surfaces using face milling process," *International Journal of Machine Tools and Manufacture*, vol. 105, pp. 32–44, 2016.
- [86] E. Oranlı, N. Gungoren, A. H. Astarace, E. Maleki, S. Bagherifard, and M. Guagliano, "Numerical and experimental analysis of sand blasting on polymeric substrates," *Forces in Mechanics*, vol. 12, p. 100208, 2023.
- [87] N. Jeziorski and C. Redenbach, "Stochastic geometry models for texture synthesis of machined metallic surfaces: Sandblasting and milling," *Journal of Mathematics in Industry*, vol. 14, no. 17, 2024.
- [88] B. Tang, L. Chen, W. Sun, and Z.-k. Lin, "Review of surface defect detection of steel products based on machine vision," *IET Image Processing*, vol. 17, no. 2, pp. 303–322, 2023.

- [89] K. Song and Y. Yan, "A noise robust method based on completed local binary patterns for hot-rolled steel strip surface defects," *Applied Surface Science*, vol. 285, pp. 858–864, 11 2013.
- [90] G. Fu, P. Sun, W. Zhu, J. Yang, Y. Cao, M. Y. Yang, and Y. Cao, "A deep-learning-based approach for fast and robust steel surface defects classification," *Optics and Lasers in Engineering*, vol. 121, pp. 397–405, 10 2019.
- [91] "Severstal: Steel defect detection - Kaggle." <https://www.kaggle.com/c/severstal-steel-defect-detection>.
- [92] X. Lv, F. Duan, J.-j. Jiang, X. Fu, and L. Gan, "Deep metallic surface defect detection: The new benchmark and detection network," *Sensors*, vol. 20, no. 6, 2020.
- [93] D. Tabernik, S. Šela, J. Skvarč, and D. Skočaj, "Segmentation-based deep-learning approach for surface-defect detection," *Journal of Intelligent Manufacturing*, vol. 31, pp. 759–776, Mar 2020.
- [94] J. Božič, D. Tabernik, and D. Skočaj, "Kolektorsdd2: Mixed supervision for surface-defect detection: From weakly to fully supervised learning," *Computers in Industry*, vol. 129, 8 2021.
- [95] Z. Zhang, S. Yu, S. Yang, Y. Zhou, and B. Zhao, "Rail-5k: a real-world dataset for rail surface defects detection [unpublished]," *CoRR*, vol. abs/2106.14366, 2021.
- [96] Tianchi, "Aluminum profile surface flaw recognition dataset," 2016.
- [97] P. Bergmann, M. Fauser, D. Sattlegger, and C. Steger, "Mvtec ad — a comprehensive real-world dataset for unsupervised anomaly detection," in *2019 IEEE/CVF Conference on Computer Vision and Pattern Recognition (CVPR)*, pp. 9584–9592, 2019.
- [98] P. Mishra, R. Verk, D. Fornasier, C. Piciarelli, and G. L. Foresti, "Vt-adl: A vision transformer network for image anomaly detection and localization," in *2021 IEEE 30th International Symposium on Industrial Electronics (ISIE)*, pp. 01–06, 2021.
- [99] T. Schlagenhauf and M. Landwehr, "Industrial machine tool component surface defect dataset," *Data in Brief*, vol. 39, p. 107643, 2021.
- [100] D. Honzátko, E. Türetken, S. A. Bigdeli, L. A. Dunbar, and P. Fua, "Defect segmentation for multi-illumination quality control systems," *Machine Vision and Applications*, vol. 32, p. 118, Sep 2021.
- [101] W. Matthias, H. Tobias, and H. F. A., "Dagm: Weakly supervised learning for industrial optical inspection [dataset]," 2007.
- [102] T. Bao, J. Chen, W. Li, X. Wang, J. Fei, L. Wu, R. Zhao, and Y. Zheng, "MIAD: A maintenance inspection dataset for unsupervised anomaly detection [unpublished]," *CoRR*, vol. abs/2211.13968, 2022.
- [103] X. Zhu, T. Bilal, P. Mårtensson, L. Hanson, M. Björkman, and A. Maki, "Towards sim-to-real industrial parts classification with synthetic dataset," in *2023 IEEE/CVF Conference on Computer Vision and Pattern Recognition Workshops (CVPRW)*, pp. 4454–4463, 2023.
- [104] P. Gospodnetic, M. Rauhut, and H. Hagen, "Surface inspection planning using 3d visualization," *LEVIA*, 2020.
- [105] K. Wada, "Labelme: Image polygonal annotation with Python."
- [106] Y. Gong, G. Liu, Y. Xue, R. Li, and L. Meng, "A survey on dataset quality in machine learning," *Information and Software Technology*, vol. 162, p. 107268, 2023.
- [107] E. Wood, T. Baltrušaitis, C. Hewitt, S. Dziadzio, T. J. Cashman, and J. Shotton, "Fake it till you make it: Face analysis in the wild using synthetic data alone," in *Proceedings of the IEEE/CVF International Conference on Computer Vision (ICCV)*, pp. 3681–3691, October 2021.
- [108] J. Tremblay, A. Prakash, D. Acuna, M. Brophy, V. Jampani, C. Anil, T. To, E. Cameracci, S. Boochoon, and S. Birchfield, "Training deep networks with synthetic data: Bridging the reality gap by domain randomization," in *2018 IEEE/CVF Conference on Computer Vision and Pattern Recognition Workshops (CVPRW)*, (Los Alamitos, CA, USA), pp. 1082–10828, IEEE Computer Society, jun 2018.
- [109] A. Gaidon, Q. Wang, Y. Cabon, and E. Vig, "Virtual worlds as proxy for multi-object tracking analysis," in *2016 IEEE Conference on Computer Vision and Pattern Recognition (CVPR)*, pp. 4340–4349, 2016.
- [110] A. Farahani, S. Voghoci, K. Rasheed, and H. R. Arabnia, "A brief review of domain adaptation," in *Transactions on Computational Science and Computational Intelligence*, 2021.
- [111] Y. Ma, X. Gu, and Y. Wang, "Histogram similarity measure using variable bin size distance," *Computer Vision and Image Understanding*, vol. 114, no. 8, pp. 981–989, 2010.
- [112] Z. Wang, A. Bovik, H. Sheikh, and E. Simoncelli, "Image quality assessment: from error visibility to structural similarity," *IEEE Transactions on Image Processing*, vol. 13, no. 4, pp. 600–612, 2004.
- [113] I. Arganda-Carreras, S. C. Turaga, D. R. Berger, D. Cireşan, A. Giusti, L. M. Gambardella, J. Schmidhuber, D. Laptev, S. Dwivedi, J. M. Buhmann, T. Liu, M. Seyedhosseini, T. Tasdizen, L. Kamensky, R. Burget, V. Uher, X. Tan, C. Sun, T. D. Pham, E. Bas, M. G. Uzunbas, A. Cardona, J. Schindelin, and H. S. Seung, "Crowdsourcing the creation of image segmentation algorithms for connectomics," *Frontiers in Neuroanatomy*, vol. 9, 2015.
- [114] R. M. Haralick, K. Shanmugam, and I. Dinstein, "Textural features for image classification," *IEEE Transactions on Systems, Man, and Cybernetics*, vol. SMC-3, no. 6, pp. 610–621, 1973.
- [115] R. Zhang, P. Isola, A. A. Efros, E. Shechtman, and O. Wang, "The unreasonable effectiveness of deep features as a perceptual metric," in *2018 IEEE/CVF Conference on Computer Vision and Pattern Recognition*, pp. 586–595, 2018.
- [116] M. Heusel, H. Ramsauer, T. Unterthiner, B. Nessler, and S. Hochreiter, "GANs trained by a two time-scale update rule converge to a local nash equilibrium," in *Advances in Neural Information Processing Systems (I. Guyon, U. V. Luxburg, S. Bengio, H. Wallach, R. Fergus, S. Vishwanathan, and R. Garnett, eds.)*, vol. 30, Curran Associates, Inc., 2017.
- [117] A. Krizhevsky, I. Sutskever, and G. E. Hinton, "Imagenet classification with deep convolutional neural networks," in *Advances in Neural Information Processing Systems (F. Pereira, C. Burges, L. Bottou, and K. Weinberger, eds.)*, vol. 25, Curran Associates, Inc., 2012.
- [118] D. Hendrycks and T. Dietterich, "Benchmarking neural network robustness to common corruptions and perturbations," 2019.
- [119] A. Torralba and A. A. Efros, "Unbiased look at dataset bias," in *CVPR 2011*, pp. 1521–1528, 2011.
- [120] O. Ronneberger, P. Fischer, and T. Brox, "U-net: Convolutional networks for biomedical image segmentation," in *Medical Image Computing and Computer-Assisted Intervention – MICCAI 2015 (N. Navab, J. Hornegger, W. M. Wells, and A. F. Frangi, eds.)*, (Cham), pp. 234–241, Springer International Publishing, 2015.
- [121] K. He, X. Zhang, S. Ren, and J. Sun, "Deep residual learning for image recognition," in *2016 IEEE Conference on Computer Vision and Pattern Recognition (CVPR)*, pp. 770–778, 2016.
- [122] I. Loshchilov and F. Hutter, "Decoupled weight decay regularization," in *International Conference on Learning Representations*, 2017.